SWING domains prime chromatin for nuclear body–mediated gene regulation

Ruofan Yu, Hanna Sas-Nowosielska, Abhisha Sawant Dessai, Amal Oubarri, Hannah Kim, Christine Faunce, Benjamin Vanderkruk, Katherine A Alexander, Son C Nguyen, Ian D. Krantz, Eric F Joyce, Melike Lakadamyali and Shelley L Berger

Abstract

Nuclear speckles have long been recognized as RNA-rich nuclear bodies, yet their role in genome organization and gene regulation remains incompletely understood. Using a rapid dTAG-mediated degradation system to simultaneously deplete SON and SRRM2—the core structural components of nuclear speckles—we identify a novel class of genomic regions, which we term SWING domains. Upon speckle disruption, SWING domains relocate to the nuclear periphery and acquire repressive histone marks such as H3K9me3, accompanied by transcriptional downregulation, particularly of genes involved in developmental pathways. Notably, human mutations in SON and SRRM2 are associated with neurodevelopmental disorders characterized by intellectual disability and global developmental delay. Patient-derived cells bearing such mutations similarly exhibit SWING-domain relocalization and gene repression, underlining a role for speckles in developmental gene regulation. We also report that previously discovered drug-induced speckle rejuvenation can partially rescue aberrant SWING-domain localization to the nuclear lamina and the associated transcriptome in patient-derived cells and iPSC with acute SON depletion. These findings establish nuclear speckles as key organizers of active chromatin, functioning in opposition to repressive compartments like the nuclear lamina. Our work reveals a mechanism for how nuclear bodies contribute to 3D genome organization and highlights the importance of nuclear speckles in developmental regulation, providing potential avenues for therapeutic intervention.

Impact Statement:

1. Identification of nuclear speckles as determinants of specific 3D genome features.
2. Demonstration of functional interactions between opposing nuclear compartments through SWING domains.
3. Establishes developmental relevance of speckle-mediated genome organization.
4. Provides potential avenues for therapeutic intervention in speckleopathies.

Introduction

Nuclear bodies are membraneless, morphologically distinct sub-nuclear compartments increasingly recognized as active participants in genome function rather than passive storage depots. Among them, nuclear speckles are enriched for RNAs and RNA-processing proteins and have been implicated in both chromosome organization and gene regulation[1,2]. In parallel with broader efforts to integrate structure and function in the 4D nucleome, evidence has accumulated that speckles help coordinate transcription, splicing, 3′-end formation, and mRNA export, positioning them as dynamic hubs for gene expression[3,4].

Genomic mapping of speckles[5–8] showed that genomic regions closest to speckles—so-called speckle-associated domains (SPADs)—harbor dense clusters of actively transcribed genes and exhibit euchromatic features, including H3K27ac and H3K4me3 enrichment and robust RNA polymerase II occupancy; importantly, mean distance to speckles is a strong predictor of expression across cell types[6]. Consistent imaging and genomic analyses emphasize that speckle proximity marks transcriptionally permissive neighborhoods enriched for RNA-processing machinery and active histone modifications[5–8]. In contrast, lamina-associated domains (LADs) are depleted of active marks, enriched for repressive heterochromatin (for example, H3K9me3-associated states), and display low gene activity, underscoring a spatial and epigenetic opposition between speckle-proximal and lamina-proximal compartments[9,10]. Despite this mutual exclusivity, how the compartments are stably demarcated and whether there is an active competition between them, is not known.

Further, although there is striking correlation between SPADs and active chromatin[5–8] , mechanistic insight into how speckles contribute to chromatin organization remains lacking. Our previous work implicated chromatin architectural factors—CTCF and the cohesin subunit RAD21—in promoting speckle–chromatin association, providing evidence that speckles participate in 3D genome architecture[8] . However, relatively few perturbation studies have directly tested speckle function in active chromatin organization, and those available have generally reported only modest effects on chromatin architecture[11,12], a confounding outcome that suggests it may be necessary to look beyond active chromatin to uncover how speckles exert broad organizational roles.

It is notable that speckles appear to have profound relevance to human health. The clinical relevance of speckle integrity is highlighted by "nuclear speckleopathies": inherited human variants in core speckle components[13] , including in SON[14] and SRRM2[15] , are associated with neurodevelopmental disorders. Severe speckleopathies are characterized by intellectual disability and global developmental delay, underscoring the importance of speckles to normal human development[16].

Here, we acutely disrupt speckles via rapid dTAG-mediated co-degradation of SON and SRRM2 to map consequences for genome organization and transcription. We define a speckle-wired genomic program and reveal a class of domains that, upon speckle disruption, relocalize to the nuclear lamina, acquire repressive chromatin features, and undergo transcriptional downregulation—particularly among developmental genes. Analyses in patient-derived cells bearing SON mutation expose concordant domain relocalization and gene repression, thus linking speckle integrity to developmental gene control. Finally, we show that pharmacologic "speckle rejuvenation" can partially rescue aberrant domain localization and transcription in both patient-derived cells and an iPSC model with rapid SON degradation, suggesting potential for therapeutic intervention in speckle-associated pathologies.

Results

1. Disruption of nuclear speckles leads to increased lamina association of certain genomic domains

The core nuclear speckle components SON and SRRM2—both necessary for speckle formation[13] —are required for cell and organismal viability[17,18]. To enable temporal control of speckle disruption, we used a previously constructed K562 cell line in which both SON and SRRM2 were tagged with FKBP12, allowing acute depletion with the small molecule dTAG[11]. Depletion of both proteins was evident by 6 h of dTAG treatment and persisted for at least 24 h (Figure 1A). Nuclear speckles were effectively dispersed after 24 h of dTAG treatment; proteins normally enriched in speckles, including RBM25[19,20] and SF3a66[7] , lost their speckle-like localization and redistributed throughout the nucleoplasm with reduced granularity and more uniform distribution (Supplementary Figure 1A).

To assess changes in chromatin organization upon speckle disruption, we performed STORM (Stochastic Optical Reconstruction Microscopy) imaging of immunolabeled total histone H3. H3 protein levels remain unchanged following dTAG treatment to deplete SON/SRRM2 (Supplementary Figure 1B). We observed striking redistribution of H3 toward the nuclear periphery. To quantify the changes in chromatin organization in an unbiased fashion, we applied O-SNAP[21,22] (Objective Single Molecule Nuclear Architecture Profiler) analysis to extract 144 features representing the spatial distribution of chromatin domains within the nucleus from the STORM H3 images. This analysis revealed significant changes to chromatin domain organization at the nuclear periphery (see Supplementary Figure 1C for all imaged nuclei and Supplementary Figure 1D for summary of O-SNAP significant features), including a significant increase of the thickness of Lamin Associated Domains (LADs) modeled from the STORM images of chromatin at the nuclear periphery (Figure 1B). This analysis is consistent with increased association of chromatin with lamina-associated domains (LADs), however, with no apparent change in nuclear size (Figure 1C).

In light of this observation—that speckle disruption relocates chromatin to the lamina—we investigated whether the effect is global or confined to specific genomic regions via assaying DNA association with the lamina utilizing Lamin B1 CUT&RUN[23]. Our Lamin B1 CUT&RUN profiles showed strong technical reproducibility (Supplementary Figure 2A) and correlated well with previous Lamin B1 DamID[24], a widely used method for mapping lamina-associated regions (Supplementary Figure 2B). We also note that Lamin B1 subcellular localization and protein level were not visibly altered in 24h dTAG-treated cells (Supplementary Figure 2C-D). Upon 24 h of dTAG treatment, we observed striking gains of Lamin B1 association with specific DNA regions, rather than a global increase (Figure 1D-E). Because these regions relocate to the lamina in response to speckle disruption, we refer to them as SWING domains, highlighting their dynamic behavior (see purple region of BED tracks in Figure 1D-E). Consistently, the metagene plot and heat map show a clear increase in lamina association, represented by an increase of Lamin B1 CUT&RUN signal, within SWING domains (Figure 1F), but not within canonical LADs or speckle-associated domains (SPADs). To further substantiate this conclusion, we performed DNA-FISH to measure the distance between probe foci and the nuclear periphery. In agreement with the Lamin B1 CUT&RUN results, SWING probes relocated significantly closer to the lamina, whereas SPAD probes showed no significant movement (Figure 1G-H). In summary, we observed that a subfraction of the genome—here termed SWING domains—relocates to the nuclear lamina upon acute disruption of nuclear speckles.

2. SWING domains exhibit intermediate properties

We next investigated certain properties of SWING domains. Using previously published genomic maps of speckles (SON TSA-seq) and the nuclear lamina (Lamin B1 DamID) in K562 cell[6,24] , we found that SWING domains exhibit intermediate association level with both structures, indicating SWING is located between speckles and nuclear lamina (Figure 1I–J, Supplementary Figure 3A). To assess whether this conclusion holds cytologically, we analyzed genome-wide multiplex FISH (MERFISH) data generated in IMR90 cells[25]. Although this is a different cell line, prior work reported some conservation of both SPADs and LADs across cell lines[6,10,26] . Consistent with the genomic profiles, SWING domains in the MERFISH

117 dataset occupied intermediate distances to both speckles and the lamina (Supplementary Figure 3C–D).
118 Supporting this notion, we examined the baseline localization of SWING domains prior to dTAG-mediated
119 speckle disruption and found that the majority localize either to LADs or to intermediate regions not
120 classified as LAD or SPAD, rather than to SPADs (Fig. 1K; single-chromosome view in Supplementary
121 Fig. 3E).

122 At broader genomic scale, lamina association shows partial conservation across cell lines, with a subset of
123 lamina-associated domains (LADs) shared across cell types while other LADs are more dynamic[26]. Given
124 the SWING domain sensitivity to speckle perturbation and its intermediate nature, we investigated whether
125 the SWING domain is also more variable across cell lines. We compared published Lamin B1 association
126 profiles[24] for K562 (chronic myeloid leukemia), HFFc6 (human foreskin fibroblast), HCT116 (colorectal
127 cancer), and H1 (human embryonic stem cell) cell lines. Lamin B1 association exhibited significantly
128 higher variability (quantified as the standard deviation of the Lamin B1 signal across these four cell lines)
129 in SWING domains compared with canonical LADs and SPADs (Supplementary Figure 3F–G), and,
130 consistently, the majority of medium- to high-variability Lamin B1–associated domains across these cell
131 types reside within SWING domains (Figure 3H).

132 We next asked whether SWING domains also display intermediate chromatin architecture. Because SPADs
133 are strongly associated with the active A1 subcompartment[5,27] and LADs with the repressive B2/B3
134 subcompartment[27] , we examined subcompartment composition within SWING domains. Using published
135 Hi-C data from K562 cells[28] , we assigned genomic subcompartments[29] and observed that SWING domains
136 frequently co-occur with the intermediate A2 and B1 subcompartments (Figure 1L). Genome-wide analyses
137 further revealed that SWING domains are enriched for A2 and B1, whereas both SPADs and LADs are
138 depleted for these intermediate subcompartments (Figure 1M, Supplementary Figure 3I). Thus, even when
139 considering chromatin partitioning alone, independent of lamina or speckle association, SWING domains
140 exhibit intermediate properties that are distinct from LADs and SPADs, suggesting a unique biological role.

141 **3. SWING domain becomes more heterochromatin-like upon speckle disruption**

142 Given that SWING domains show intermediate association with the nuclear lamina and nuclear speckles,
143 we next investigated whether they also display hybrid histone modification profiles, between activation-
144 associated acetylation and repression-associated methylation. Using publicly available ENCODE ChIP–seq
145 datasets[30] from K562 cells, we quantified the distribution of six histone modifications (Figure 2A). For all
146 six modifications, SWING domains showed signal levels between those observed in LADs and SPADs.
147 Notably, SWING regions exhibited intermediate enrichment for the facultative heterochromatin mark
148 H3K27me3 and the constitutive heterochromatin mark H3K9me3 (Figure 2A). These two modifications
149 form an interlaced pattern within SWING domains, in contrast to the more uniform distribution of
150 H3K27me3 in SPADs and H3K9me3 in LADs (sample region in Figure 2B). Together, these patterns
151 indicate that SWING domains represent an intermediate chromatin state bridging constitutive and
152 facultative heterochromatin.

153 We next examined whether acute speckle disruption alters H3K27me3 and H3K9me3 distribution.
154 Immunofluorescence in cells with or without dTAG-mediated speckle disruption showed that H3K27me3
155 remained broadly evenly dispersed across the nucleus, whereas H3K9me3 showed striking redistribution
156 toward the nuclear periphery (Figure 3C; quantification in Figure 3D). Because SWING domains relocalize
157 to the nuclear lamina—a nuclear context associated with H3K9me3 deposition—we examined whether
158 these changes occur specifically within SWING. We utilized CUT&RUN profiling for H3K27me3 and
159 H3K9me3 and focused on the SWING set defined previously (Figure 1). There was a decrease in
160 H3K27me3 at both SWING and SPAD (example tracks in Figure 2E; genome-wide quantification in Figure
161 2F) and, in contrast, an increase in H3K9me3 that was specific to SWING (Figure 2E, G). Beyond changes

in signal magnitude, most regions with significant gained H3K9me3 mapped to SWING (Figure 2H, left), showing a clear enrichment (Figure 2I). We also detected an enrichment for depleted H3K27me3 across SWING, albeit weaker than for gained H3K9me3 (Figure 2H, right; Figure 2I). Together, the increased H3K9me3 and reduced H3K27me3 indicate that, upon acute speckle disruption, SWING chromatin shifts towards a constitutive heterochromatin-like state.

4. Nuclear Speckle Disruption leads to down-regulation of SWING genes

We next investigated whether the increased lamina association and gain of repressive H3K9me3 in SWING domains upon acute speckle depletion led to gene repression. We performed RNA-seq in K562 cells with 24 h of dTAG treatment to disrupt nuclear speckles or DMSO control. As quality control, we observed a general shift toward gene downregulation in dTAG-treated samples (Supplementary Figure 4A). We report that LADs, SWING, and SPADs show increasing numbers of expressed genes and increasing basal expression (Supplementary Figure 4B), consistent with previous observations that gene expression increases with speckle association and decreases with lamina association[5] . Consistent with prior reports that speckles promote expression of speckle-associated genes[7,8,31,32] , genes in SPADs were predominantly downregulated upon speckle disruption (Figure 3A-B). Strikingly, genes in SWING domains were also significantly downregulated, and to an even greater extent than were SPAD genes (Figure 3A-B). This difference was not explained by baseline expression: in an expression-matched analysis, SWING genes still showed a stronger tendency toward downregulation than SPAD genes (Figure 3C). SWING-domain genes formed a distinct cluster among differentially expressed genes in both hierarchical clustering heatmap and volcano plot in comparison with SPAD genes (Figure 3D-E). Genome browser views further illustrate these trends: genes with increased Lamin B1 CUT&RUN signal tended to be downregulated, particularly within SWING domains (e.g., LINC02794 and CYP39A1), whereas genes in regions without increased Lamin B1 were unchanged or upregulated (e.g., FAAH and POLH) (Figure 3F). Of note, because very few LAD genes are expressed in these cells, they were excluded from this comparison.

Beyond the well-documented role of speckles in promoting transcription of SPAD genes, our data indicate that speckles also regulate genes in SWING domains, which lie at intermediate distances from speckles, potentially via a distinct mechanism. Because SPAD genes are enriched in cellular processes requiring high basal and/or rapid expression[6,33] (e.g., housekeeping and stress-response pathways), we investigated whether genes within SWING domains also encompass preferential pathway associations. Motif analysis across all identified SWING domain revealed that top-ranked transcription factors enriched include developmental regulators, such as the embryonic and cell-fate determinant SOX7[34] and the homeobox factor SIX1[35] (Figure 3G). Consistently, gene ontology analysis of SWING-localized genes showed significant enrichment for development-related pathways (Supplementary Figure 4C). In addition, genes downregulated upon acute speckle disruption were significantly enriched for nervous system and circulatory system development terms (Figure 3H). Together, these results suggest that, in contrast to SPAD genes that require high basal and/or rapid expression, SWING genes are subject to developmentally induced activation or repression and are particularly sensitive to speckle-mediated control, potentially enabling finer spatial and temporal regulation characteristic of developmental programs.

5. SWING domains relocate away from the lamina upon LMNA disruption

Building on our finding that SWING domains relocalize toward the nuclear lamina after speckle disruption—accompanied by increased H3K9me3 and gene downregulation—we investigated whether speckles and the lamina might actually "compete" for association at SWING domains. Prior studies suggest that speckle- and lamina-associated chromatin are largely mutually exclusive[24,27], raising a question of whether "swinging" occurs bidirectionally, in particular whether weakening the nuclear lamina tethering relocates SWING domains away from the lamina and potentially toward speckles.

Lamina association is mediated predominantly by two factors, the Lamin B receptor (LBR) and Lamin A/C (LMNA), which engage distinct tethering mechanisms[36]. Although their genome-wide occupancy is broadly similar[37] , perturbation studies show factor-specific sensitivity: LBR loss tends to cause widespread LAD detachment, whereas LMNA loss appears, on average, milder[24]. To test how each factor affects SWING domain localization, we reanalyzed published Lamin B1 DamID datasets from K562 cells bearing CRISPR-mediated knockouts of LBR or LMNA[24], using the LAD/SWING/SPAD annotations defined with our double dTAG system. We observed that LMNA knockout produced a selective reduction of lamina association in SWING domains, with minimal change across canonical LADs or SPADs (Figure 4A; genome-wide summary in Figure 4B). In contrast, LBR knockout caused a global decrease in lamina association across LADs but a relative increase in lamina association within SWING domains (Figure 4A–B). Differential analysis of Lamin B1 signal confirmed that most regions changing in LMNA mutants map to SWING, and these changes are directionally opposite in LMNA versus LBR backgrounds (heatmap of CUT&RUN differential regions in Figure 4C; genome wide quantification in Figure 4D). Together, these results indicate that, among the two lamina tethering factors, LMNA specifically counterbalances speckle association at SWING domains, while LBR primarily maintains broad LAD tethering.

We investigated whether these localization changes translate into altered gene expression. Consistent with the localization shift, genes located in regions that show a significant decrease in Lamin B1 association in LMNA reduction were downregulated upon speckle disruption (Figure 4E, dTAG; see Figure 4F for representative Lamin B1 DamID and RNA-seq coverage). However, these genes were significantly upregulated only in the LMNA mutant (Figure 4E, LMNA; p-values from one-sample tests against zero are shown), with no significant change in the LBR mutant (Figure 4E, LBR). These inverse effects support a competitive model in which speckles and LMNA establishing opposite regulatory influences on SWING-domain genes. In summary, our data support a bidirectional "swinging" of SWING domains between speckles and the lamina: speckle disruption relocates SWING domains toward the lamina, leading to gene repression, whereas LMNA loss relocates SWING domains away from the lamina, leading to gene de-repression.

6. Speckle activation by drug treatment reduces lamina tethering

Hence, loss of lamina tethering, specifically via LMNA disruption, relocalizes SWING domains away from the nuclear lamina. We investigated whether a speckle gain-of-function would produce a similar outcome. A recent study identified the FDA-approved small molecule pyrvinium pamoate (PP) as a speckle gain-of-function treatment that increases speckle volume and mimics the transcriptional response of SON overexpression by lowering the surface tension of an intrinsically disordered region in SON[38]. Those findings demonstrate robust speckle enlargement in mouse embryonic fibroblasts and human iPSC-derived neurons. We tested this phenotype in K562 cells: PP treatment markedly increased both individual speckle size and speckle number for SON and the speckle-localized factor RBM25 (Figure 5A). Using STORM imaging, we further observed that cells treated with 100 nM PP, despite having similar nuclear size, exhibited a significant reduction in LAD thickness (Figure 5B-5C, see Supplementary Figure 5A for all imaged nuclei and 5B for summary of O-SNAP significant features)—the exact opposite of the LAD thickening observed upon dTAG-mediated speckle disruption (Figure 1B-1C).

Mutations in the speckle core proteins SON and SRRM2 are associated with neurodevelopmental disorders; SON mutations cause Zhu–Tokita–Takenouchi–Kim (ZTTK) syndrome[14] , and SRRM2 mutations are linked to a yet-unnamed developmental disorder[15] . Affected individuals show overlapping phenotypes, including developmental delay, distinctive facial features, and intellectual disability, supporting a hypothesis that speckle dysfunction can lead to a group of neurodevelopmental pathologies, or "nuclear speckleopathies"[16] . Our findings above reveal that speckles regulate SWING domains which are enriched for developmental pathways. Thus, we next investigated: (1) whether cells derived from patients with

253 mutations in speckle genes exhibit aberrant gains in lamina association, and (2) whether pharmacological
254 speckle activation can restore speckle morphology and function in these patient-derived cells. We analyzed
255 blood-derived lymphoblastoid cell lines (LCLs) from two patients: one carrying a premature stop-gain
256 mutation in SON (P276; c.3334C>T; Sanger validation in Figure 5D; patient ontology terms in
257 Supplementary Figure 6A), and the other carrying a premature stop-gain mutation in SRRM2 (P246;
258 c.1117C>T; Sanger validation in Supplementary Figure 6B; patient ontology terms in Supplementary
259 Figure 6C). Consistent with the genotype, SON expression in P276 was ~50% of control by RNA-seq
260 (Supplementary Figure 6D), and SRRM2 expression in P246 was similarly ~50% of control
261 (Supplementary Figure 6E). Immunofluorescence revealed smaller nuclear speckle area in both P246 and
262 P276 compared with a healthy donor LCL (S1) (Figure 5E; quantification in Figure 5F–G). We then treated
263 cells with pyrvinium pamoate (PP) and found that the reduced speckle area in both patient cell lines showed
264 a trend toward restoration (Figure 5F; S1 vs. P276+PP and S1 vs. P246+PP).

265 We then performed Lamin B1 CUT&RUN in both patient cell lines. Consistent with our K562 dTAG results
266 (Figure 1), both P276 (SON mutation; browser view in Figure 5H; genome-wide summary in Figure 5I)
267 and P246 (SRRM2 mutation; browser view in Supplementary Figure 7A; genome-wide summary in
268 Supplementary Figure 7B) showed aberrant increases in lamina association specifically within SWING
269 domains, with little or no change across canonical LADs or SPADs. Approximately 50% of SWING
270 domains identified in the two patient lines overlap (Figure 5J), suggesting that SON and SRRM2 regulate
271 chromatin positioning through a similar mechanism. SWING domains identified in P276 significantly
272 overlapped those defined in K562 (Figure 5K) and were similarly highly enriched for nervous system
273 development pathway genes (Supplementary Figure 7C).

274 Notably, 100 nM PP treatment reduced the aberrant Lamin B1 association in P276 (example locus in Figure
275 5H; genome-wide summary in Figure 5I; heatmap of all Lamin B1 differential regions in Figure 5M).
276 Across all SWING domains in P276, nearly half were rescued by PP (Figure 5L), and reciprocally, the
277 majority of PP-rescued regions fell within SWING (Figure 5M, left) compared with LAD (Figure 5M,
278 right). We also note that although aberrant lamina association was apparent in P246 with the SRRM2
279 mutation, the rescue effect of PP was not obvious in terms of Lamin B1 signal (Supplementary Figure 7A–
280 B), potentially because PP has been proposed to act primarily through SON rather than SRRM2[38] .

281 In summary, patient cells harboring disease-causing mutations in SON or SRRM2 exhibit abnormal
282 increases in chromatin–lamina associations; in P276, this phenotype was mitigated by PP treatment,
283 consistent with speckle activation restoring both speckle morphology and lamina association toward a
284 healthy state.

285 **7. Developmental pathway dysregulation in speckleopathy patient cells is mitigated by pyrvinium**
286 **pamoate**

287 We next investigated whether the aberrant lamina association observed in the patient lines—and its partial
288 reversal by PP—extends to transcriptional changes. We performed RNA-seq in LCLs from a healthy donor
289 (S1) and from P276 and P246.

290 For P276, genes located within SWING domains (the regions showing aberrant lamina gain) were
291 overwhelmingly downregulated relative to S1 (distribution in Figure 6A; domain-focused comparison in
292 Figure 7B). Compared with SPAD or LAD genes—of which about half were significantly downregulated
293 versus upregulated—more than 90% of SWING genes were downregulated (Figure 6C; heatmap in Figure
294 6D). These data mirror our acute speckle disruption results in K562 (Figure 3).

295

For P246, we observed the same pattern: SWING genes were strongly downregulated relative to S1 (Supplementary Figure 8A–B), whereas SPAD and LAD genes showed a roughly balanced mix of down- and upregulation (Supplementary Figure 8C). Together, these findings indicate that SWING genes are highly sensitive to speckle-mediated control in a patient context with long-term speckle dysfunction.

We next assessed whether PP treatment modulates gene expression at loci with aberrant lamina gain that were rescued at the chromatin level. Because robust PP-mediated rescue was observed only in P276 (Figure 5H), we focused our analysis on this cell line. Across genes within PP-rescued regions, we observed a modest upward shift in expression (Figure 6E). Although the aggregate change did not reach statistical significance, the small number of expressed genes in this subset (n = 47) likely limits power. Focusing on genes meeting a stringent rescue criterion (significantly downregulated in P276 vs S1 and significantly upregulated in P276+PP vs P276 at FDR < 0.1), we identified several developmentally relevant genes, including the G protein–coupled receptor ADGRA3, the homeobox transcription factor MEIS2, and HDAC9, which is implicated in cardiac muscle development (example locus in Figure 6G). Gene Ontology analysis of PP-rescued genes showed enrichment for nervous system development terms (Figure 6H). The overall magnitude of rescue was limited, which is expected given the low baseline expression of developmental programs in non-differentiating K562 and LCL models, limiting the ability for detection of robust transcriptional restoration.

In summary, disruption of nuclear speckles repositions SWING domains toward the nuclear lamina, where H3K9me3 accumulates and genes are inhibited. In contrast, loss of Lamin A/C or speckle activation by PP shifts SWING domains toward speckles, alleviating lamina tethering and favoring gene activation. Together, these reciprocal mechanisms coordinate chromatin positioning and gene regulation to dynamically modulate developmental pathways (Figure 6I).

8. Pyrvinium pamoate rescues early neurodevelopmental gene expression in iPSCs with acute SON depletion

Given that K562 and LCL models are not in a developmental context, limiting our ability to capture transcriptional changes, we therefore sought to investigate the transcriptional consequences of speckle disruption during development and its potential restoration with PP. To facilitate this, we developed an induced pluripotent stem cell (iPSC) model bearing FKBP12-tagged SON, enabling rapid degradation. After 24 h of dTAG treatment, SON was nearly eliminated by immunofluorescence (Figure 7A; broader view in Supplementary Figure 9A) and by Western blot (Figure 7B). Notably, SON depletion caused a marked change in SRRM2-labeled speckle morphology: speckles became significantly smaller and rounder (Figure 7A; quantification in Figure 7C), consistent with prior reports that SON is a core component required for normal speckle formation[13] . Additionally, consistent with reports that SON is essential for cell and organismal viability, high-dose dTAG treatment (500 nM for 24 h) caused extensive cell-cycle arrest at metaphase (Figure 7D; broader view in Supplementary Figure 7B; quantification in Figure 7E, comparing DMSO to 500 nM dTAG).

We next tested whether PP rescues speckle morphology and the metaphase-arrest phenotype in SON-depleted iPSCs. Treatment with 50 nM PP alone did not alter speckle morphology (Figure 7A; quantification in Figure 7C, DMSO vs PP) or the fraction of cells in metaphase (Figure 7D; quantification in Figure 7E). In SON-depleted cells, PP did not rescue speckle morphology under complete depletion (compare 500 nM dTAG to 500 nM dTAG + PP), which is consistent with reports that PP acts by altering the biophysical properties of SON[38] ; accordingly, when no SON protein remains, little or no morphological rescue is expected. PP did, however, reduce the metaphase-arrest fraction across dTAG concentrations (Figure 7E). When we gradually reduced the dTAG concentration to achieve partial depletion, we observed robust restoration—both in speckle morphology (Figure 7C; Supplementary Figure 9C–E) and in the

341 proportion of cells in metaphase, with both metrics returned to near-DMSO levels at 7.8 nM dTAG (Figure
342 7E).

343 We continued with partial depletion at 7.8 nM dTAG (full depletion at 500 nM caused cell death, consistent
344 with prior reports that SON is essential for cell survival) to test how SON depletion—and PP rescue—
345 affects the developmental transcriptome. Because SON mutations cause ZTTK syndrome with a
346 characteristic neurodevelopmental phenotype, we induced iPSC-to-neuron differentiation by doxycycline
347 activation of an NGN2 construct in SON–FKBP12 iPSCs. iPSCs were treated for 24 h with DMSO, dTAG,
348 PP, or dTAG+PP, followed the next day (Day 0) by doxycycline induction; RNA-seq sample was harvested
349 at Day0 and after 1 day of differentiation (Day 1; schematic in Figure 7F). We did not extend the experiment
350 beyond day 2 because substantial cell death occurred even at 7.8 nM dTAG. Nevertheless, by day 1 we
351 observed robust induction of neuronal lineage and neuronal differentiation genes in DMSO controls (Day
352 1 vs Day 0; transcriptome distributions in Figure 7G; Gene Ontology analysis in Supplementary Figure 9F).
353 We refer to these as early neuronal differentiation (early-ND) genes.

354 We next investigated whether SON depletion affects expression of the early-ND genes. Comparing day 1
355 dTAG with day 1 DMSO cells, the majority of early-ND genes (64.7%) were downregulated, whereas
356 genome-wide DEGs were roughly evenly split between up- and downregulation (Figure 7H; compare early-
357 ND vs other genes), indicating that loss of speckle integrity selectively impairs neuronal differentiation
358 gene expression. We then asked whether PP rescues the impaired induction of early-ND genes (i.e., early-
359 ND genes with FC < 0 in Figure 7H) by comparing day 1 dTAG+PP vs dTAG. Because PP is known to
360 inhibit mitochondrial respiration[39,40] , we controlled for PP's non-speckle mediated effects by calculating a
361 PP-rescue contrast in the dTAG background (see Methods for details). Using this control, we found that the
362 vast majority of early-ND genes (73.4%) showed restored expression (Figure 7I, "ND"; heatmap of
363 significant early-ND genes in Figure 7J; summary quantification in Figure 7K), whereas non-ND genes
364 ("other") did not show this trend.

365 Notably, multiple dTAG-impaired and PP-rescued genes are established neuronal lineage factors
366 (highlighted in red in Figure 7J), including the glycosyltransferase LFNG (early neuronal commitment),
367 NNAT (neurite outgrowth and early neurodevelopment), and ZEB1 (neural progenitor marker) (Figure 7L).
368 Collectively, these results show that (1) SON depletion selectively impairs neuronal differentiation
369 programs, and (2) PP treatment selectively rescues these pathways during iPSC-to-iNeuron differentiation.

370 **Discussion**

371 In this study, we identify a novel class of genomic regions—which we term SWING domains—that are
372 sensitive to speckle dysfunction: either acute depletion in engineered cells or by clinical patient-derived
373 mutations in speckle components relocates these domains towards the nuclear lamina. This repositioning is
374 accompanied by increased H3K9me3 and preferential downregulation of genes residing in SWING
375 domains, which are enriched for developmental pathways. We further show that nuclear lamina component
376 Lamin A/C competes with speckles for SWING positioning and regulation: Lamin A/C loss shifts SWING
377 away from the lamina and induces the opposite transcriptional response, indicating inverse control by
378 speckles and Lamin A/C. Finally, as proof of principle, pharmacological speckle activation with pyrvinium
379 pamoate partially corrects both nuclear architecture—by reducing aberrant lamina association—and
380 expression of a subset of developmentally relevant genes in patient cells and in iPSC model with acute SON
381 depletion. These findings suggest the possibility of drug-mediated modulation of nuclear body–chromatin
382 interactions to mitigate specific consequences of speckle-related dysfunction (Figure 7M).

383 Our study identifies nuclear speckles as determinants of specific genome features and, for the first time,
384 shows that disrupting speckles directly alters chromatin organization by increasing nuclear lamina

385 association (Figure 1). Although speckles are long correlated with active chromatin, the evidence is largely
386 correlational, with direct perturbation tests previously limited. Prior work used siRNA against SRRM2 in
387 a mouse cell line[12] , or a 6-hour acute co-degradation of SON and SRRM2 followed by 3D-genome readouts
388 (HiChIP)[11] ; in these studies there were minimal global changes in contacts. In contrast, we reveal that the
389 effects of speckle disruption are not genome-wide but rather concentrated in a defined subset of regions—
390 the SWING domains. This domain specificity, and the partial or short-term nature of earlier perturbations,
391 likely explains limited changes detected previously.

392 Our results also demonstrate competition for chromatin association of SWING domains between nuclear
393 speckles and the nuclear lamina (Figure 5). Building on the inverse correlation between speckle and lamina
394 association observed across cell lines[6,27] , we show that this competition specifically involves speckles and
395 lamin A/C—but not LBR— although lamin A/C and LBR are both major mediators of chromatin–lamina
396 interactions. This is consistent with prior observations that lamin A/C–sensitive LADs are more facultative
397 and variable, whereas LBR-dependent LADs are more constitutive[36,41]. Notably, lamin A/C can exist in a
398 nucleoplasmic pool[42] , potentially regulated by phosphorylation[43] which could be relevant to the flux of
399 SWING domains. Overall, the molecular mechanism underlying this competition remains to be determined.

400 We establish that, in addition to regulating speckle-associated (SPAD) genes, nuclear speckles also regulate
401 non-speckle-associated genes within SWING domains via a distinct mechanism. Prior work shows that
402 speckles facilitate expression of speckle-proximal genes such as p53 targets[31] and HIF-2α targets[32] ,
403 potentially by enhancing splicing efficiency[7]. Our results extend this model: speckles also compete with
404 nuclear lamina mediated repression of non-speckle-associated SWING genes, limiting deposition of
405 repressive marks such as H3K9me3 (Figure 3). We also find pathway differences between SWING domains
406 and SPAD: SPAD genes are enriched for housekeeping and stress-response functions, whereas SWING
407 domains appear to be enriched for developmental pathways (Figure 4G–H). We therefore hypothesize that,
408 unlike SPAD genes that may require high basal and/or rapid expression, SWING genes could occupy an
409 intermediate regulatory state that is particularly sensitive to speckle-mediated control, potentially enabling
410 finer spatial and temporal regulation characteristic of developmental programs.

411 Multiple reports implicate mutations in nuclear speckle components, including SON and SRRM2 in
412 neurodevelopmental disease[14–16]. In a clinical context using patient-derived cell lines, we observed that
413 speckle dysfunction caused by naturally occurring mutations also led to aberrant lamina association, and
414 correlated repression of SWING genes (Figure 6-7). We further found that treatment with pyrvinium
415 pamoate (PP)—a small molecule drug reported to function by modifying biophysical properties of an
416 intrinsically disordered region (IDR) of SON[38] —rescued aberrant lamina association and partially
417 improved transcriptomic readouts in both patient derived cell line model and in iPSC with acute SON
418 depletion. We acknowledge that PP is likely not sufficiently specific for speckles, given its known inhibition
419 of mitochondrial respiration, and that substantial work remains before any clinical application. Even so, our
420 findings point to intriguing therapeutic possibilities: small-molecule compounds and other approaches that
421 modulate the biophysical properties of nuclear body components—including peptides and nanobodies—
422 may partially restore nuclear-body function in disease contexts.

423 **References**

424 1. Spector, D. L. & Lamond, A. I. Nuclear Speckles. *Cold Spring Harb. Perspect. Biol.* **3**, a000646
425 (2011).

426 2. Galganski, L., Urbanek, M. O. & Krzyzosiak, W. J. Nuclear speckles: molecular organization,
427 biological function and role in disease. *Nucleic Acids Res.* **45**, 10350–10368 (2017).

428 3. Consortium, 4D Nucleome *et al.* An integrated view of the structure and function of the human 4D
429 nucleome. *bioRxiv* 2024.09.17.613111 (2024) doi:10.1101/2024.09.17.613111.

430 4. Faber, G. P., Nadav-Eliyahu, S. & Shav-Tal, Y. Nuclear speckles – a driving force in gene expression.
431 *J. Cell Sci.* **135**, (2022).

432 5. Chen, Y. *et al.* Mapping 3D genome organization relative to nuclear compartments using TSA-Seq as a
433 cytological ruler. *J. Cell Biol.* **217**, 4025–4048 (2018).

434 6. Zhang, L. *et al.* TSA-seq reveals a largely conserved genome organization relative to nuclear speckles
435 with small position changes tightly correlated with gene expression changes. *Genome Res.* **31**, 251–264
436 (2021).

437 7. Bhat, P. *et al.* Genome organization around nuclear speckles drives mRNA splicing efficiency. *Nature*
438 **629**, 1165–1173 (2024).

439 8. Yu, R. *et al.* CTCF/RAD21 organize the ground state of chromatin–nuclear speckle association. *Nat.*
440 *Struct. Mol. Biol.* **32**, 1–12 (2025).

441 9. Guelen, L. *et al.* Domain organization of human chromosomes revealed by mapping of nuclear lamina
442 interactions. *Nature* **453**, 948–951 (2008).

443 10. Steensel, B. van & Belmont, A. S. Lamina-Associated Domains: Links with Chromosome
444 Architecture, Heterochromatin, and Gene Repression. *Cell* **169**, 780–791 (2017).

445 11. Roseman, S. A. *et al.* DNA methylation insulates genic regions from CTCF loops near nuclear
446 speckles. *eLife* **13**, RP102930 (2025).

447 12. Hu, S., Lv, P., Yan, Z. & Wen, B. Disruption of nuclear speckles reduces chromatin interactions in
448 active compartments. *Epigenetics Chromatin* **12**, 43 (2019).

449 13. Ilik, İ. A. *et al.* SON and SRRM2 are essential for nuclear speckle formation. *eLife* **9**, e60579 (2020).

450 14. Dingemans, A. J. M. *et al.* Establishing the phenotypic spectrum of ZTTK syndrome by analysis of 52
451 individuals with variants in SON. *Eur. J. Hum. Genet.* **30**, 271–281 (2022).

452 15. Cuinat, S. *et al.* Loss-of-function variants in SRRM2 cause a neurodevelopmental disorder. *Genet.*
453 *Med.* **24**, 1774–1780 (2022).

454 16. Regan-Fendt, K. E. & Izumi, K. Nuclear speckleopathies: developmental disorders caused by variants
455 in genes encoding nuclear speckle proteins. *Hum. Genet.* **143**, 529–544 (2024).

456 17. Arafeh, R., Shibue, T., Dempster, J. M., Hahn, W. C. & Vazquez, F. The present and future of the
457 Cancer Dependency Map. *Nat. Rev. Cancer* **25**, 59–73 (2025).

458 18. Vukadin, L. *et al.* A mouse model of Zhu-Tokita-Takenouchi-Kim syndrome reveals indispensable
459 SON functions in organ development and hematopoiesis. *JCI Insight* **9**, e175053 (2024).

460 19. Thul, P. J. *et al.* A subcellular map of the human proteome. *Science* **356**, (2017).

461 20. Zhou, A., Ou, A. C., Cho, A., Benz, E. J. & Huang, S.-C. Novel Splicing Factor RBM25 Modulates
462 Bcl-x Pre-mRNA 5′ Splice Site Selection. *Mol. Cell. Biol.* **28**, 5924–5936 (2008).

463 21. Kim, H. H. *et al.* O-SNAP: A comprehensive pipeline for spatial profiling of chromatin architecture.
464 *bioRxiv* 2025.07.18.665612 (2025) doi:10.1101/2025.07.18.665612.

465 22. Dhankhar, M. *et al.* Revealing the biophysics of lamina-associated domain formation by integrating
466 theoretical modeling and high-resolution imaging. *Nat. Commun.* **16**, 7909 (2025).

467 23. Ahanger, S. H. *et al.* Distinct nuclear compartment-associated genome architecture in the developing
468 mammalian brain. *Nat. Neurosci.* **24**, 1235–1242 (2021).

469 24. Gholamalamdari, O. *et al.* Major nuclear locales define nuclear genome organization and function
470 beyond A and B compartments. *eLife* **13**, RP99116 (2025).

471 25. Su, J.-H., Zheng, P., Kinrot, S. S., Bintu, B. & Zhuang, X. Genome-Scale Imaging of the 3D
472 Organization and Transcriptional Activity of Chromatin. *Cell* **182**, 1641-1659.e26 (2020).

473 26. Meuleman, W. *et al.* Constitutive nuclear lamina–genome interactions are highly conserved and
474 associated with A/T-rich sequence. *Genome Res.* **23**, 270–280 (2013).

475 27. Wang, Y. *et al.* SPIN reveals genome-wide landscape of nuclear compartmentalization. *Genome Biol.*
476 **22**, 36 (2021).

477 28. Siegenfeld, A. P. *et al.* Polycomb-lamina antagonism partitions heterochromatin at the nuclear
478 periphery. *Nat. Commun.* **13**, 4199 (2022).

479 29. Liu, Y. *et al.* Systematic inference and comparison of multi-scale chromatin sub-compartments
480 connects spatial organization to cell phenotypes. *Nat. Commun.* **12**, 2439 (2021).

481 30. Luo, Y. *et al.* New developments on the Encyclopedia of DNA Elements (ENCODE) data portal.
482 *Nucleic Acids Res.* **48**, D882–D889 (2019).

483 31. Alexander, K. A. *et al.* p53 mediates target gene association with nuclear speckles for amplified RNA
484 expression. *Mol. Cell* **81**, 1666-1681.e6 (2021).

485 32. Alexander, K. A. *et al.* Nuclear speckles regulate functional programs in cancer. *Nat. Cell Biol.* **27**,
486 322–335 (2025).

487 33. Kim, J., Venkata, N. C., Gonzalez, G. A. H., Khanna, N. & Belmont, A. S. Gene expression
488 amplification by nuclear speckle association. *J. Cell Biol.* **219**, e201904046 (2019).

489 34. Stovall, D. B., Cao, P. & Sui, G. SOX7: from a developmental regulator to an emerging tumor
490 suppressor. *Histol. Histopathol.* **29**, 439–45 (2013).

491 35. Zheng, W. *et al.* The role of Six1 in mammalian auditory system development. *Dev. (Camb., Engl.)*
492 **130**, 3989–4000 (2003).

493 36. Solovei, I. *et al.* LBR and Lamin A/C Sequentially Tether Peripheral Heterochromatin and Inversely
494 Regulate Differentiation. *Cell* **152**, 584–598 (2013).

495 37. Wong, X. *et al.* Mapping the micro-proteome of the nuclear lamina and lamina-associated domains.
496 *Life Sci. Alliance* **4**, e202000774 (2021).

497 38. Dion, W. *et al.* SON-dependent nuclear speckle rehabilitation alleviates proteinopathies. *Nat.*
498 *Commun.* **16**, 7065 (2025).

499 39. Ishii, I., Harada, Y. & Kasahara, T. Reprofiling a classical anthelmintic, pyrvinium pamoate, as an
500 anti-cancer drug targeting mitochondrial respiration. *Front. Oncol.* **2**, 137 (2012).

501 40. Xiang, W. *et al.* Pyrvinium selectively targets blast phase-chronic myeloid leukemia through
502 inhibition of mitochondrial respiration. *Oncotarget* **6**, 33769–33780 (2015).

503 41. Kind, J. *et al.* Genome-wide Maps of Nuclear Lamina Interactions in Single Human Cells. *Cell* **163**,
504 134–147 (2015).

505 42. Muralikrishna, Bh. *et al.* Immunolocalization of detergent-susceptible nucleoplasmic lamin A/C foci
506 by a novel monoclonal antibody. *J. Cell. Biochem.* **91**, 730–739 (2004).

507 43. Ikegami, K., Secchia, S., Almakki, O., Lieb, J. D. & Moskowitz, I. P. Phosphorylated Lamin A/C in
508 the Nuclear Interior Binds Active Enhancers Associated with Abnormal Transcription in Progeria. *Dev.*
509 *Cell* **52**, 699-713.e11 (2020).

510 44. Otterstrom, J. *et al.* Super-resolution microscopy reveals how histone tail acetylation affects DNA
511 compaction within nucleosomes in vivo. *Nucleic Acids Res.* **47**, 8470–8484 (2019).

512 45. Nguyen, S. C. & Joyce, E. F. Programmable Chromosome Painting with Oligopaints. *Methods Mol.*
513 *Biol. (Clifton, NJ)* **2038**, 167–180 (2019).

514 46. Petrovic, J. *et al.* Oncogenic Notch Promotes Long-Range Regulatory Interactions within
515 Hyperconnected 3D Cliques. *Mol. Cell* **73**, 1174-1190.e12 (2019).

516 47. Stirling, D. R. *et al.* CellProfiler 4: improvements in speed, utility and usability. *BMC Bioinform.* **22**,
517 433 (2021).

518 48. Levet, F. *et al.* SR-Tesseler: a method to segment and quantify localization-based super-resolution
519 microscopy data. *Nat. Methods* **12**, 1065–1071 (2015).

520 49. Xu, S., Grullon, S., Ge, K. & Peng, W. Spatial clustering for identification of ChIP-enriched regions
521 (SICER) to map regions of histone methylation patterns in embryonic stem cells. *Methods Mol. Biol.*
522 *(Clifton, NJ)* **1150**, 97–111 (2014).

Acknowledgments

We thank Dr. Brian Liau and Dr. Shelby Roseman for generously providing the SON/SRRM2 double-dTAG K562 cell line, and Dr. Andrew Belmont and Dr. Bas van Steensel for generously providing the LMNA and LBR knockout K562 cells, and Dr. Ian Krantz for providing all LCL lines used in this study.

Material and Methods

This research complies with all relevant ethical regulations for studies involving cultured human cell lines by University of Pennsylvania.

Experimental methods

Cell culture

K562 derivatives—SON/SRRM2 FKBP12 double knock-in, LMNA knockout (LMNA−/−), and LBR knockout (LBR−/−)—were maintained in RPMI-1640 containing 2 mM L-glutamine (Invitrogen, 11875085), 10% fetal bovine serum (FBS), and 1% penicillin–streptomycin at 37 °C with 5% CO_2. Lymphoblastoid cell lines (LCLs) were cultured in RPMI-1640 supplemented with 10% FBS and 1% penicillin–streptomycin under identical conditions. Human iPSCs were maintained on Matrigel-coated plates (Corning, hESC-qualified, 354277) in Essential 8 Medium (Gibco/Thermo Fisher Scientific, A1517001) with daily medium changes at 37 °C, 5% CO_2. Cells were passaged at ~70–80% confluency using ReLeSR (STEMCELL Technologies, 05872) for clumps or Accutase for single cells (Innovative Cell Technologies, AT104), with 10 μM Y-27632 ROCK inhibitor added after thawing or single-cell passage (Tocris, 1254).

For acute speckle disruption, cells were treated with 500 nM dTAG v1 (Tocris 6914) for 24 h unless otherwise indicated; matched DMSO (Sigma D8418) vehicle controls were included. For pharmacologic speckle activation, pyrvinium pamoate (PP, Sigma P0027) was applied at 100 nM for 24 h unless noted.

All experiments used independently grown and treated biological replicates. Cell line identity and genotype were confirmed by Sanger sequencing and/or immunoblotting against the relevant tagged proteins. Cultures were routinely screened and found negative for mycoplasma contamination at least every six months.

iPSC to iNeuron Differentiation

iPSCs were differentiated to iNeurons on poly-D-lysine/laminin–coated plates (PDL, Sigma P0899-10MG; laminin, Life Technologies 23017-015). DMSO, PP or dTAG were added at Day -1. From Day 0–Day1, cells were transitioned to a KOSR-based medium (KnockOut DMEM 10829-018, KSR 10828028, NEAA 10370088, GlutaMAX 35050061, β-ME 21985023) and induced with dual-SMAD inhibition plus Wnt blockade (LDN-193189, DNSK 1062368-24-4, 100 nM; SB431542, Tocris 1254, 10 μM; XAV939, Stemgent 04-00046, 2 μM) together with doxycycline to activate NGN2 (Sigma D9891-1G, 2 μg/mL).

Western blotting

Samples were lysed with RIPA buffer (150nM NaCl, 1% IGEPAL, 0.5% sodium deoxycholate, 0.1% SDS and 50mM Tris pH7.4). Protein concentration was determined by bicinchoninic acid assay (BCA) protein assay (#23227, Life Technologies). Samples were separated using precast 4-12% Bis-Tris

polyacrylamide gels (ThermoFisher Scientific, NP0321BOX) in the presence of SDS. Proteins were transferred to nitrocellulose membrane, blocked with 5% milk TBST and probed with designated primary antibodies overnight at 4°C. Following TBST wash steps, membranes were incubated in secondary goat anti rabbit antibody (1:10000, Bio-Rad, 1706515) for one hour, washed with TBST, and detected using using Thermo Scientific SuperSignal West Pico PLUS Chemiluminescent Substrate (ThermoFisher Scientific, 34577). Signal quantification was performed using ImageJ software.

Immunofluorescence and antibodies

Cells were washed twice with PBS and fixed with Paraformaldehyde solution 4% in PBS (Santa Cruz Biotechnology, CAS 30525-89-4) for 10 minutes at room temperature, washed again with PBS (Corning, 21-031-CV) then permeated with 0.1% PBS Triton X-100 for 15 minutes. Cells were incubated overnight in primary antibodies targeting GFP to stain GFP labelled SON (abcam, ab121759) or SRRM2 (Sigma-Aldrich, S4045) diluted 1:200 in PBS at 4C. Secondary antibody conjugated with Goat anti-Rabbit IgG Alexa Fluor™ 488 (ThermoFisher Scientific, A-11008) and Goat anti-Mouse IgG Alexa Fluor™ 647 (ThermoFisher Scientific, A-21235) were diluted 1:200 in PBS and used respectively. After 1 hour incubation at room temperature, samples were washed and incubated in 1:10000 DAPI (Invitrogen, D1306, 5 mg/mL) for 5min. Imaging was performed with Nikon Eclipse Ti2 widefield microscope. Cells were imaged at focal plane with a 40x objective, and a deep depletion CCD camera cooled to between -70 and -80C.

Stochastic Optical Reconstruction Microscopy (STORM) imaging

Immunofluorescence was performed as described previously and in[44] , using a 1:50 dilution of anti-H3 primary antibody (Active Motif, 39763) and a 1:50 dilution of Alexa Fluor™ 647–conjugated secondary antibody (Thermo Fisher Scientific, A-21235) in PBS. STORM imaging was performed as described in the literature[21] . Briefly, images were acquired on an ONI Nanoimager (Oxford Nanoimaging) controlled by NimOS software (v1.19.4) using the 640-nm laser (exciting AF647). Cells were imaged in buffer containing 0.1 M cysteamine (MEA; 77 mg/mL stock; Sigma-Aldrich, 30070-10G prepared in 360 mM HCl; Fisher, A508-P500), 5% (w/v) glucose (Alfa Aesar, A16828), and a 1% GLOX solution. The GLOX solution was prepared by dissolving 14 mg glucose oxidase (Sigma-Aldrich, G2133) in 50 µL catalase (20 mg/mL; Roche, 106810) and bringing to 200 µL with 10 mM Tris (pH 8.0; Invitrogen, 15568025) containing 50 mM NaCl (Fisher, S217-500). Imaging buffer was replaced every 90 min. Acquisition settings were 15-ms exposure for 30,000 frames at 30 °C with constant high-intensity illumination at 647-nm excitation.

Oligopaint DNA-FISH

Sample slides were fixed with 4% PFA in PBS for 10 minutes at room temperature, washed with PBS and permeabilized with 0.5% Triton in PBS for 15 minutes. Subsequently, DNA-FISH was performed as described[45]. Oligopaint DNA-FISH probes to target genes were designed across a 50kb region centered on the transcription start site as described[46]. Imaging was performed with Nikon Eclipse Ti2 widefield microscope. Cells were imaged at focal plane with a 40x objective.

CUT&RUN sequencing

CUT&RUN was performed as described previously with minor modification[23]. For each condition, nuclei from ~6×10^5 cells were isolated in nuclear isolation buffer (10 mM HEPES-KOH pH 7.9, 10

mM KCl, 0.1% NP-40, 0.5 mM spermidine, 1× Halt protease inhibitor cocktail) and bound to concanavalin A–coated magnetic beads (BioMag Plus) pre-equilibrated in binding buffer (20 mM HEPES-KOH pH 7.9, 10 mM KCl, 1 mM $CaCl_2$, 1 mM $MnCl_2$). After bead binding, samples were split for antibody incubations; binding buffer was replaced with primary antibody diluted 1:100 in blocking buffer (20 mM HEPES-KOH pH 7.5, 150 mM NaCl, 0.1% BSA, 0.5 mM spermidine, 1× Halt protease inhibitor cocktail, 2 mM EDTA). Normal IgG (Millipore 06-371) was included as a negative control. Bead–nuclei were rotated overnight at 4 °C, washed in washing buffer (20 mM HEPES-KOH pH 7.5, 150 mM NaCl, 0.1% BSA, 0.5 mM spermidine, 1× Halt protease inhibitor cocktail), and incubated with pA-MNase on ice. Digestion was initiated by addition of $CaCl_2$ and carried out for 30 min on a pre-chilled metal block on ice. Reactions were stopped by adding STOP buffer (200 mM NaCl, 20 mM EDTA, 4 mM EGTA, 50 µg/mL RNase A, 40 µg/mL glycogen) with gentle vortexing, followed by fragment release at 37 °C for 10 min. Supernatants were collected, treated with Proteinase K at 70 °C for 10 min, and DNA was purified by phenol:chloroform:isoamyl alcohol extraction. Libraries were prepared from released DNA using the NEBNext Ultra II DNA Library Prep Kit for Illumina, size profiles were assessed on an Agilent TapeStation, and concentrations quantified with the NEBNext Library Quant Kit (E7630, NEB). Libraries were sequenced on an Illumina NextSeq 1000 using NextSeq™ 1000/2000 P2 XLEAP-SBS™ Reagent Kit with 61bp per read.

Polyadenylated RNA-seq

Cells were lysed in TRIzol (15596018, Thermo Fisher Scientific) and snap frozen. RNA was then isolated using chloroform extraction, followed by Zymo Direct-zol RNA Miniprep Kits (Zymo Research, R2050), including DNA digestion with DNase. Poly(A)+ RNA was further isolated using double selection with poly-dT beads (E7490, NEB). RNA-seq libraries were prepared using the NEBNext Ultra II Directional Library Prep Kit for Illumina (E7760, NEB). The size of the libraries was determined using a Bioanalyzer, and their concentration was determined using the NEBNext Lib Quant Kit (E7630, NEB). Libraries were sequenced on an Illumina NextSeq 1000 using NextSeq™ 1000/2000 P2 XLEAP-SBS™ Reagent Kit with 61bp per read.

Data processing and analysis

Statistics & Reproducibility

Details of the statistical tests are documented in the sections below for each analysis. For all replicate experiments in this study, cells were grown and treated separately as biological replicates. No statistical methods were used to pre-determine sample sizes, but our sample sizes are similar to those reported in previous publications [6,31]. For all image-based statistics apart from STORM (see corresponding section for details), two-sided Wilcoxon test was performed, and no assumption of data distribution was made.

Immunofluorescence (IF) data processing and analysis

All IF images were taken at the focal plane with the autofocus function of Nikon NIS software (5.30.04) on a Nikon Eclipse Ti2 widefield microscope, except for the STORM imaging in Figure 1B and 6B. Subsequent image processing was performed with CellProfiler[47] (version 4.2.1, https://cellprofiler.org/) to identify nuclear speckle and measure various size, shape and intensity parameters. Pipeline and notes are available on Github: https://githu.com/Chalietia/CellProfiler/.

DNA-FISH processing and analysis

Images were preprocessed (flat-field correction and background subtraction) and analyzed in CellProfiler (version 4.2.1) with custom pipelines available at https://github.com/Chalietia/CellProfiler. Nuclei were segmented from DAPI using adaptive thresholding and size/shape filters to remove debris and touching clumps. DNA-FISH foci were detected per nucleus using a Laplacian-of-Gaussian spot detector with intensity and size thresholds chosen from control images; nuclei harboring >4 foci (indicative of over-segmentation or multiplets) were excluded a priori. Distances were measured in pixels and converted to physical units using the system pixel size (0.16 µm/pixel). Distance distributions were summarized as medians with interquartile ranges and compared across conditions using two-sided Mann–Whitney–Wilcoxon tests; where multiple comparisons were performed, p-values were adjusted by the Benjamini–Hochberg method.

STORM imaging analysis

Localizations at the nucleus were manually segmented from the field of view. The local compaction maps of the STORM image data were generated using Voronoi tessellation as previously described[48] , where each Voronoi cell is pseudo-colored based on its respective area. In addition to the maps, O-SNAP (Objective Single-Molecule Nuclear Architecture Profiler; https://github.com/LakGroup/O-SNAP) was performed on the H3 localization data as described in the literature[21]. Briefly, the pipeline extracts 144 features from single molecule localization data. The features describe properties such as nucleus morphology as well as global and local organization of the H3 signal. O-SNAP then conducts parallel, orthogonal analyses to perform feature exploration. A volcano analysis identifies features that change most dramatically between experimental groups based on fold change and statistical significance using Welch's t-test with the Benjamini-Hochberg method for multiple test correction. Here, O-SNAP highlights the modeled LAD thickness; the process for generating these modeled LAD segments is originally described in literature[22].

CUT&RUN data processing

Sequencing reads were aligned to the human reference genome GRCh38/hg38 using Bowtie2 v2.3.4.1 with the following parameters: --very-sensitive-local --no-mixed --no-discordant -I 10 -X 1000 -x hg38. Alignments were filtered with samtools v1.1 (view -q 5), sorted and indexed, and PCR duplicates were removed with Picard v2.26 (MarkDuplicates, REMOVE_DUPLICATES=true). Reads mapping to ENCODE hg38 blacklist regions were excluded from all downstream analyses (hg38 blacklist v2). Signal tracks (bigWig/bedGraph) were generated with deepTools (bamCompare) using -bs 5000 --smoothLength 15000 --effectiveGenomeSize 2913022398 --exactScaling --normalizeUsing RPKM --scaleFactorsMethod None -bl <hg38_blacklist.bed>, comparing each target to its matched IgG control.

CUT&RUN/DamID differential analysis and SWING domain definition

Differential analysis followed a published sliding-window framework[31] (step-by-step: https://github.com/katealexander/TSAseq-Alexander2020/tree/master/genomicBins_DiffBind) with minor modifications. Briefly, PCR-deduplicated BAMs (targets with matched inputs/controls) were quantified over 50-kb windows tiled across hg38 at a 5-kb step (1/10 window) using DiffBind v3.12.0 (https://bioconductor.org/packages/release/bioc/html/DiffBind.html) with input subtraction enabled. Custom blacklist regions (generated as described above) and ENCODE hg38 blacklist were supplied to DiffBind via dba.blacklist(). Library-size normalization used DBA_NORM_RLE. Windows

showing significant SON signal change (FDR < 0.01, Benjamini–Hochberg) were split by direction and merged into contiguous intervals with BEDTools (merge) to yield differential domains. For SWING domain calls, differential regions exhibiting a significant increase in Lamin B1 signal (FDR < 0.01) in K562 dTAG-treated versus control, or in patient (P276) versus healthy donor (S1), were designated as SWING domains. Genes were assigned to domains by intersecting domain intervals with transcription start sites; genes whose TSS fell within a differential domain were extracted using a Python script adapted from getGenesWithin.py in the referenced workflow.

LAD and SPAD calling

Broad domains were called with SICER2 (v1.1) [49] on hg38 using the following assay-matched controls: matched IgG for CUT&RUN, no-primary control for TSA-seq, and no-Dam (Dam-only) control for DamID: sicer -t <signal.bam> -c <control.bam> -s hg38 -fdr 0.1 -w 2000 -g 20000. For SPADs, <signal> was SON CUT&RUN or SON TSA-seq libraries; for LADs, <signal> was Lamin B1 CUT&RUN or Lamin B1 DamID, as indicated. Resulting BED files were sorted and filtered to remove ENCODE hg38 blacklist regions. Consensus domains for each condition were defined by strict replication: domains present in all biological replicates were intersected with bedtools (intersect, optionally followed by merge to consolidate adjacent fragments), and the shared overlap was taken as the final set for downstream analyses. When LAD/SPAD domains overlapped SWING domains, SWING regions were given precedence and corresponding overlapping region is removed by bedtools subtract. Overlapping bases were removed from the LAD/SPAD sets using bedtools subtract followed by sorting.

Gene ontology (GO) analysis

Gene sets comprising (i) genes of which TSSs reside within SWING domains and/or (ii) genes with significant differential expression by RNA-seq (as described in Results) were analyzed with STRING (https://string-db.org/; organism: Homo sapiens) using default enrichment settings. GO Biological Process terms were tested with STRING's built-in over-representation analysis and Benjamini–Hochberg multiple-testing correction; terms with FDR < 0.05 were considered significant. To reduce redundancy, significant terms were clustered by similarity at a threshold of 0.8, and representative terms were reported. Unless fewer were available, the first 10 significant (non-redundant) terms are shown. Input identifiers were supplied as official gene symbols, and background was set to the STRING genome-wide reference.

RNA-seq processing and differential analysis

Reads were aligned to the human reference genome GRCh38/hg38 with STAR v2.7.1a (https://github.com/alexdobin/STAR) using:--outFilterType BySJout --outFilterMultimapNmax 20 --alignSJoverhangMin 8 --alignSJDBoverhangMin 1 --outFilterMismatchNmax 999 --outFilterMismatchNoverReadLmax 0.04 --alignIntronMin 20 --alignIntronMax 1000000.Alignments were quantified to RefSeq gene models (GRCh38) using htseq-count (v0.11.1) in union mode (--type exon --idattr gene_id -s no). Gene-level normalization and differential expression were performed with DESeq2 (v1.40.2) using default settings (size-factor normalization; Wald test; Benjamini–Hochberg adjustment). Unless otherwise indicated, genes with FDR < 0.05 and absolute log2 fold change >1 were considered differentially expressed. Statistical differences between log2 fold changes of predefined gene groups were assessed using two-sided Mann–Whitney–Wilcoxon tests; where multiple comparisons were made, p-values were adjusted by the Benjamini–Hochberg method.

Identifying PP-rescued gene in iPSC to early iNeuron differentiation

For rescue analyses (day 1 only), RNA-seq counts were modeled with DESeq2 using within-day contrasts to estimate a PP-specific rescue effect while controlling for PP's baseline impact. We defined the rescue contrast as $R_{\mathrm{PP}} = (\text{dTAG+PP vs dTAG}) - (\text{PP vs DMSO})$, which measures the incremental effect of PP in the dTAG background after subtracting PP's standalone effect. Positive R_{PP}values indicate PP-mediated restoration of expression beyond its baseline action, whereas negative values indicate the opposite. Significance was assessed by DESeq2's Wald test with Benjamini–Hochberg adjustment, and interpretations in the text and figures refer to this day-1 contrast.

Figure legends

Figure 1. Disruption of nuclear speckles increases lamina association of specific genomic domains.

(A) Western blot of FKBP12-tagged core speckle proteins SON and SRRM2 after the indicated durations of dTAG treatment; GAPDH serves as a loading control.

(B) Representative STORM image from K562 SON/SRRM2 double knock-in cells with or without dTAG treatment for 24hr; the color scale encodes log10 Voronoi polygon area.

(C) Quantification of nuclear area (left) and LAD thickness (right) from STORM datasets. Box plots show the median and interquartile range (IQR); whiskers extend to 1.5× IQR. P-values were computed using two-sided Welch's t-tests with Benjamini–Hochberg correction for multiple comparisons.

(D–E) Representative genome browser tracks (three biological replicates per condition) for DMSO and dTAG-treated samples. Red arrows mark regions with increased lamina association upon dTAG treatment. Bottom tracks indicate domain calls: LAD (red), SWING (purple), and SPAD (blue). A zoomed-out view of the light-blue highlighted region is shown at right.

(F) Metagene profiles and heatmaps of Lamin B1 CUT&RUN signal across all called LADs, SWING domains, and SPADs in DMSO versus dTAG-treated K562 cells.

(G–H) (Top) DNA-FISH images using probes targeting a SPAD locus (cyan) and a SWING locus (magenta) in DMSO- or dTAG-treated cells. (Bottom) Corresponding Lamin B1 CUT&RUN browser tracks and quantification of 3D distances from FISH signals to the nuclear periphery. Box plots as in (C); *P* values by two-sided Mann–Whitney *U* test. Each dot represents one FISH foci.

(I–J) Quantification of speckle association (SON TSA-seq signal; A) and nuclear lamina association (Lamin B1 DamID signal; B) across LADs, SWING domains, and SPADs in K562 cells. Violin plots show distributions with embedded box plots (median, IQR; whiskers 1.5× IQR) where applicable. *P* values are from two-sided Mann–Whitney U tests.

(K) Distribution of lamin-associated domains (LADs), speckle-associated domains (SPADs), and intermediate regions (not classified as LAD or SPAD) in baseline K562 cells, shown genome-wide ("All") and within SWING domains.

(L) Representative view in K562 cells showing Lamin B1 CUT&RUN signal, corresponding SWING domain calls, and Hi-C subcompartment annotations.

(M) Distribution (% of bases) of A1, A2, B1, and B2 subcompartments genome-wide (All) and within LADs, SWING domains, and SPADs in K562 cells.

Figure 2. SWING domains become more heterochromatin-like upon speckle disruption.

(A) Percentile distributions of designated histone-modification ChIP–seq signals across LADs, SWING domains, and SPADs.

(B) Example browser view of H3K27me3 and H3K9me3 CUT&RUN signal in control K562 cells. BED tracks indicate domain calls: LAD (red), SWING (purple), SPAD (blue).

(C) Representative IF images for H3K9me3 and H3K27me3 in K562 cells with or without 24 h dTAG treatment.

(D) Quantification of distances from the nuclear periphery for regions classified as H3K9me3 or H3K27me3 in K562 cells with or without 24 h dTAG treatment. Box plots show the median and interquartile range (IQR); whiskers extend to 1.5× IQR. P values by two-sided Mann–Whitney U tests.

(E) Example browser view of H3K27me3 and H3K9me3 CUT&RUN signal in K562 cells with or without 24 h dTAG treatment; blue arrows indicate regions with reduced signal and red arrows indicate regions with increased signal.

(F–G) Metagene profiles and heatmaps of H3K27me3 (F) and H3K9me3 (G) CUT&RUN signal across all called LADs, SWING, and SPADs in DMSO versus dTAG-treated K562 cells. Metagene lines show mean normalized CUT&RUN signal with shaded 95% CI; heatmaps display z-scored signal per region, centered at region midpoints and ordered by mean signal.

(H) Percentages of (left) all differential regions and up-regulated H3K9me3 regions and (right) all differential regions and down-regulated H3K27me3 regions within LADs, SWING domains, and SPADs. Bars show category proportions.

(I) Enrichment of H3K9me3-upregulated regions and H3K27me3-downregulated regions across LADs, SWING, and SPADs, reported as log2 (observed/expected).

Figure 3. Nuclear speckle disruption leads to down-regulation of SWING genes.

(A) Comparison of significantly differentially expressed genes (FDR < 0.05 and |log2 fold change| > 1) between dTAG 24 h and DMSO in K562 cells, grouped by localization (SPAD vs SWING). Box plots show median and IQR; whiskers, 1.5× IQR. P values by two-sided Mann–Whitney U tests.

(B) Percentile distributions showing the proportions of significantly down-regulated (blue) and up-regulated (red) genes within SPAD or SWING.

(C) Distributions of log2 fold change for expression-matched SPAD versus SWING genes (no FDR or fold-change cutoff). Lines show mean with shaded 95% CI.

(D) RNA-seq heatmap of all significantly differentially expressed genes (FDR < 0.05 and |log2 fold change| > 1) in SWING and SPAD with hierarchical clustering. The y-axis lists individual genes; SPAD genes are labeled blue and SWING genes purple. Values are z-scores of normalized RNA-seq counts.

(E) Volcano plot for K562 cells treated with dTAG (24 h) versus DMSO. Points are colored by domain localization (SPAD, blue; SWING, purple). "Sig" indicates significantly differentially expressed genes (FDR < 0.05 and |log2 fold change| > 1); "NS" indicates not significant. The panel above shows density distributions for the designated gene groups.

(F) Example browser view showing Lamin B1 CUT&RUN tracks and normalized RNA-seq counts for genes within SPAD (FAAH, POLH) and within SWING (LINC02794, CYP39A1). The "domain" BED track indicates calls: LAD (red), SWING (purple), SPAD (blue).

(G) HOMER motif-enrichment results for SWING domains; entries highlighted in red denote development-related transcription factors.

(H) Gene Ontology Biological Process enrichment for significantly decreased SWING genes (FDR < 0.05 and log2 fold change < −1) in dTAG 24 h versus DMSO K562 cells; development-related terms are highlighted.

854 **Figure 4. SWING domains relocate away from the lamina upon LMNA disruption.**
855
856 **(A)** Representative genome browser view of Lamin B1 DamID signal in WT, LMNA KO, and LBR KO
857 K562 cells. Blue arrows mark regions with decreased lamina association; red arrows mark regions with
858 increased lamina association in the indicated genotype. Bottom tracks indicate domain calls: LAD (red),
859 SWING (purple), SPAD (blue). A zoomed-out view of the light-blue highlighted region is shown at right.
860
861 **(B)** Metagene profiles and heatmaps of Lamin B1 DamID signal across all called LADs, SWING domains,
862 and SPADs in WT, LMNA KO, and LBR KO K562 cells.
863
864 **(C)** Heatmap of z-score–normalized Lamin B1 DamID signal in WT, LMNA KO, and LBR KO K562 cells
865 with hierarchical clustering, grouped by domain category (LAD, red; SWING, purple; SPAD, blue).
866
867 **(D)** Proportions (%) of significantly increased or decreased Lamin B1–associated regions in LBR KO (left)
868 and LMNA KO (right), colored by domain category (LAD, red; SWING, purple; SPAD, blue). Bars show
869 category proportions.
870
871 **(E)** Comparison of log2 fold change in gene expression across K562 conditions—dTAG-mediated speckle
872 disruption, LMNA KO, and LBR KO—for genes that show significantly decreased Lamin B1 association
873 (FDR < 0.01) in LMNA KO cells. Box plots show median and IQR; whiskers, 1.5× IQR.
874
875 **(F)** Example browser view showing Lamin B1 DamID tracks and normalized RNA-seq counts for indicated
876 genes; light-blue shading highlights gene bodies.
877

878 **Figure 5. Speckle activation by drug treatment reduces lamina tethering in patient derived cells.**
879
880 **(A)** Left: representative IF images in K562 cells under the indicated treatments and antibodies. Right:
881 quantification of speckle area and speckle count per nucleus. Box plots show median and IQR; whiskers,
882 1.5× IQR. P values by two-sided Mann–Whitney U tests.
883
884 **(B)** Representative STORM image from K562 SON/SRRM2 double knock-in cells with or without PP
885 (pyrvinium pamoate) treatment; the color scale encodes log10 Voronoi polygon area.
886
887 **(C)** Quantification of nuclear area (left) and LAD thickness (right) from STORM datasets. Box plots as in
888 (A). P values by two-sided Welch's t-tests with Benjamini–Hochberg correction for multiple comparisons.
889
890 **(D)** Sanger sequencing of the SON locus in a healthy control and patient 276; red arrow indicates the
891 heterozygous point mutation.
892
893 **(E)** Representative IF for SRRM2 in LCLs from a healthy donor and patient 276 (P276), with or without
894 100 nM PP.
895
896 **(F–G)** Quantification of speckle area (F) and speckle count (G) per nucleus for IF in the indicated cell lines
897 and conditions. Box plots as in (A); P values by two-sided Mann–Whitney U tests.
898
899 **(H)** Representative genome browser view of Lamin B1 CUT&RUN signal in healthy donor (S1), patient
900 276 (P276), and P276 treated with 100 nM PP. Blue arrows mark regions with decreased lamina association;
901 red arrows mark regions with increased lamina association in the indicated sample. Bottom tracks indicate
902 domain calls: LAD (red), SWING (purple), SPAD (blue). A zoomed-out view of the light-blue highlighted
903 region is shown at right.
904
905 **(I)** Metagene profiles and heatmaps of Lamin B1 CUT&RUN signal across all called LADs, SWING
906 domains, and SPADs, in S1, P276, and P276 with 100 nM PP. Metagene lines show mean normalized
907 signal; heatmaps display z-scored signal per region, centered at region midpoints and ordered by mean
908 signal.
909
910 **(J)** Overlap between SWING domains identified in patient 246 and in patient 276. P value by
911 hypergeometric test using the hg38 mappable genome as background.
912
913 **(K)** Overlap between SWING domains identified in K562 and in patient 276. P value by hypergeometric
914 test using the hg38 mappable genome as background.
915
916 **(L)** Overlap between SWING domains and regions showing significant rescue of aberrant Lamin B1 under
917 PP treatment in patient 276. P value by hypergeometric test using the hg38 mappable genome as background.
918
919 **(M)** Heatmap of z-score–normalized Lamin B1 signal across all P276+PP versus P276 differential regions
920 (FDR < 0.01) in the indicated samples, with hierarchical clustering.
921

Figure 6. Developmental pathway dysregulation in speckleopathy patient cells is mitigated by pyrvinium pamoate.

(A) Volcano plot of RNA-seq differential analysis between patient 276 (P276) and healthy donor (S1). Points are colored by domain localization (SPAD, blue; SWING, purple; LAD, red). "Sig" denotes significantly differentially expressed genes (FDR < 0.05 and |log2 fold change| > 1); "NS" denotes not significant. Axes: x, log2 fold change; y, −log10 FDR. The panel above shows density distributions for the designated gene groups.

(B) Comparison of significantly differentially expressed genes (FDR < 0.05 and |log2 fold change| > 1) between P276 and S1, grouped by localization (SPAD, SWING and LAD). Box plots show median and IQR; whiskers, 1.5× IQR. P values by two-sided Mann–Whitney U tests.

(C) Percentile distributions showing the proportions of significantly down-regulated (blue) and up-regulated (red) genes within SPAD, SWING or LAD.

(D) RNA-seq heatmap of all significantly differentially expressed genes in SWING, SPAD and LAD with hierarchical clustering between P276 and S1. The y-axis lists individual genes; Values are z-scores of normalized RNA-seq counts (per-gene z-scaling; distance = 1 − Pearson correlation; average linkage).

(E) Comparison of log2 fold change relative to S1 for genes that show Lamin B1 rescue under PP (100 nM) in P276 (untreated) versus P276+PP. P values by two-sided Wilcoxon signed-rank test.

(F) RNA-seq heatmap of genes with Lamin B1 rescue under PP that are significantly affected by PP (FDR < 0.10); development-related genes are highlighted in red.

(G) Example browser view showing Lamin B1 CUT&RUN tracks and normalized RNA-seq counts for indicated genes; light-blue shading highlights gene bodies.

(H) Gene Ontology Biological Process enrichment for genes rescued by PP (RNA-seq: P276+PP vs P276, FDR < 0.10 and fold change > 0; Lamin B1 CUT&RUN: decreased Lamin B1 in P276+PP vs P276, FDR < 0.01). Development-related terms are highlighted.

(I) Schematic illustrating the model of joint regulation of SWING domains by nuclear speckles and nuclear lamina.

Figure 7. Acute SON depletion impairs transcriptional programs during iPSC to iNeuron differentiation and is rescued by pyrvinium pamoate.

(A) Representative immunofluorescence (IF) images of iPSC SON–FKBP12 cells under the indicated treatments and stains.

(B) Western blot for SON in iPSC SON–FKBP12 cells after 24 h treatments; GAPDH serves as a loading control.

(C) Quantification of nuclear speckle area and eccentricity per nucleus from IF in (A). Box plots show median and interquartile range (IQR); whiskers, 1.5× IQR. P-values by two-sided Mann–Whitney U test.

(D) DAPI images of iPSCs under the indicated treatments (PP = 50 nM). Metaphase cells are circled in white.

(E) Fraction of metaphase cells under the indicated conditions. Error bars indicate SD. P-values by two-sided Mann–Whitney U test.

(F) Schematic of the iPSC to early iNeuron differentiation timeline.

(G) Volcano plot for RNA-seq: day 1 post doxycycline-induced differentiation vs. day 0. Highlighted genes meet FDR < 0.01 and |log2 fold change| > 1.5. Axes: x, log2 fold change; y, −log10(FDR). Top panel, density distributions for all differentially expressed genes.

(H) Volcano plot for RNA-seq: day 1 dTAG vs. day 1 DMSO. Highlighted genes are early neuronal differentiation (ND) genes upregulated in (G) (log2 fold change > 1, FDR < 0.01). “Sig” denotes significantly differentially expressed genes (FDR < 0.05 and |log2 fold change| > 1). Top panel, density distributions for designated groups.

(I) Volcano plot showing PP rescue in dTAG: rescue statistic R_PP = (dTAG+PP vs. dTAG) − (PP vs. DMSO). Highlighted genes are early ND genes whose induction is impaired by dTAG in (H) (log2 fold change < −1, FDR < 0.05). “Sig” denotes significantly rescued genes (FDR < 0.05 and |log2 fold change| > 0.5). Top panel, density distributions for designated groups.

(J) RNA-seq heatmap of all significantly PP-rescued genes (FDR < 0.05 and |log2 fold change| > 1) with hierarchical clustering. Values plotted are the average Δ normalized counts under each treatment (day 1 − day 0). The y-axis lists individual genes.

(K) Comparison of log2 fold change (day 1 vs. day 0) across conditions: control, dTAG, and dTAG+PP. for the PP-rescued gene set in (J). P-values by two-sided Wilcoxon signed-rank test.

(L) Δ normalized RNA-seq counts (day 1 − day 0) for representative genes under the indicated conditions.

(M) Model: speckle disruption impairs induction of developmental gene programs and neuronal differentiation, suggesting a potential therapeutic window for speckle-activating interventions (e.g., PP).

Supplementary Figure legends

Supplementary Figure 1.

(A) Representative images (left) and quantification (right) of IF-derived granularity and radial coefficient of variation for four nuclear speckle–localized factors—SON, SRRM2, RBM25, and SF3A66—in K562 cells with or without 24 h dTAG treatment. Violin plots show distributions with embedded box plots (median, IQR; whiskers, 1.5× IQR). P-values by two-sided Mann–Whitney U tests.

(B) Western blots for H3 and SRRM2 in K562 cells with or without dTAG treatment; GAPDH serves as a loading control. Box plots summarize band intensities (median, IQR; whiskers, 1.5× IQR). P-values by two-sided Student's t-test assuming equal variances.

(C) STORM images of K562 SON/SRRM2 double knock-in cells with (top) or without (bottom) 24 h dTAG treatment; the color scale encodes log10(Voronoi polygon area).

(D) Output from O-SNAP analysis of STORM datasets comparing cells with or without dTAG treatment, showing all significant terms (padj < 0.05).

Supplementary Figure 2.

(A) Representative genome browser tracks for three biological replicates of DMSO-treated K562 cells (left) and pairwise Pearson correlation among the three replicates (right).

(B) Representative genome browser tracks of Lamin B1 DamID and Lamin B1 CUT&RUN in K562 cells (left) and Pearson correlation between DamID and CUT&RUN signals (right).

(C) Representative IF images of Lamin B1 in K562 cells with or without 24 h dTAG treatment.

(D) Western blot for Lamin B1 in the indicated samples; GAPDH serves as a loading control. Box plots summarize band intensities (median, IQR; whiskers, 1.5× IQR). P-values by two-sided Student's t-test assuming equal variances.

Supplementary Figure 3.

(A) 2D density plot showing Lamin B1 level (x-axis) versus SON–TSA-seq signal (y-axis) for LADs, SWING domains, and SPADs. 2D density plots display kernel density estimates.

(B–C) Multiplex DNA-FISH (MERFISH) in IMR90 cells quantifying foci-to-speckle distance (B) and foci-to-lamina distance (C) for loci in LADs, SWING domains, and SPADs.

(D) 2D density plot of MERFISH measurements for loci classified as LAD, SWING, or SPAD.

(E) Distribution of lamin-associated domains (LADs), speckle-associated domains (SPADs), and intermediate regions (not classified as LAD or SPAD) in baseline K562 cells, shown genome-wide ("All") and within SWING domains on each chromosome.

(F) Example browser view of Lamin B1 DamID signal across four cell lines; bottom red track shows the per-bin standard deviation across cell lines. BED tracks indicate domain calls: LAD (red), SWING (purple), SPAD (blue).

(G) Variability of Lamin B1 signal across four cell lines, summarized as standard deviation within LADs, SWING domains, and SPADs.

(H) Proportions of low-, mid-, and high-variability regions (bottom, middle, and top tertiles by standard deviation) within LAD, SWING, and SPAD categories.

(I) Distribution (% of bases) of A1, A2, B1, and B2 subcompartments genome-wide (All) and within LADs, SWING domains, and SPADs in K562 cells.

Supplementary Figure 4.

(A) Volcano plot of RNA-seq differential expression in K562 (dTAG 24 h vs DMSO). Genes with FDR < 0.05 and |log2 fold change| > 1 are considered significant. Axes: x, log2 fold change; y, −log10 FDR.

(B) Comparison of expression levels for genes located in LAD, SWING, and SPAD in DMSO-treated K562 cells. Box plots show median and IQR; whiskers, 1.5× IQR.

(C) Gene Ontology Biological Process enrichment for all genes located in SWING domains identified in K562 cells; selected development-related terms are highlighted.

Supplementary Figure 5.

(A) STORM images of 24 hr PP treated K562 cells; the color scale encodes log10(Voronoi polygon area).

(B) Output from O-SNAP analysis of STORM datasets comparing cells with or without PP treatment, showing all significant terms (padj < 0.05).

Supplementary Figure 6.

(A) Human Phenotype Ontology (HPO) terms annotated for patient 276.

(B) Sanger sequencing of the SRRM2 locus in a healthy control and patient 246; red arrow indicates the heterozygous point mutation.

(C) Human Phenotype Ontology (HPO) terms annotated for patient 246.

(D) RNA-seq normalized counts for SON transcripts in healthy control and patient 276. Box plots show median and IQR; whiskers, 1.5× IQR.

(E) RNA-seq normalized counts for SRRM2 transcripts in healthy control and patient 246. Box plots show median and IQR; whiskers, 1.5× IQR.

Supplementary Figure 7.

(A) Representative genome browser view of Lamin B1 CUT&RUN signal in healthy donor (S1), patient 246 (P246), and P246 treated with 100 nM PP. Blue arrows mark regions with decreased lamina association; red arrows mark regions with increased lamina association in the indicated sample. Bottom tracks indicate domain calls: LAD (red), SWING (purple), SPAD (blue). A zoomed-out view of the light-blue highlighted region is shown at right.

(B) Metagene profiles and heatmaps of Lamin B1 CUT&RUN signal across all called LADs, SWING domains, and SPADs, in S1, P246, and P246 with 100 nM PP. Metagene lines show mean normalized signal; heatmaps display z-scored signal per region, centered at region midpoints and ordered by mean signal.

(C) Gene Ontology Biological Process enrichment for genes located in SWING domain identified in P276.

Supplementary Figure 8.

(A) Volcano plot of RNA-seq differential analysis between patient 246 (P246) and healthy donor (S1). Points are colored by domain localization (SPAD, blue; SWING, purple; LAD, red). "Sig" denotes significantly differentially expressed genes (FDR < 0.05 and |log2 fold change| > 1); "NS" denotes not significant. Axes: x, log2 fold change; y, −log10 FDR. The panel above shows density distributions for the designated gene groups.

(B) Comparison of significantly differentially expressed genes (FDR < 0.05 and |log2 fold change| > 1) between P246 and S1, grouped by localization (SPAD, SWING and LAD). Box plots show median and IQR; whiskers, 1.5× IQR. P values by two-sided Mann–Whitney U tests.

(C) Percentile distributions showing the proportions of significantly down-regulated (blue) and up-regulated (red) genes within SPAD, SWING or LAD.

Supplementary Figure 9.

(A) Zoomed-out immunofluorescence images corresponding to Figure 7A for DMSO and dTAG (500 nM).

(B) Zoomed-out DAPI images corresponding to Figure 7D.

(C–E) Quantification of nuclear speckle area, extent, and eccentricity per nucleus from IF across the indicated extended dTAG concentrations. Box plots show median and interquartile range (IQR); whiskers, 1.5× IQR.

(F) Gene Ontology Biological Process enrichment for genes significantly upregulated (FDR < 0.01 and |log2 fold change| > 1.5) between day 1 and day 0 post dox treatment in DMSO-treated iPSCs. Neurodevelopment-relevant pathways are highlighted.

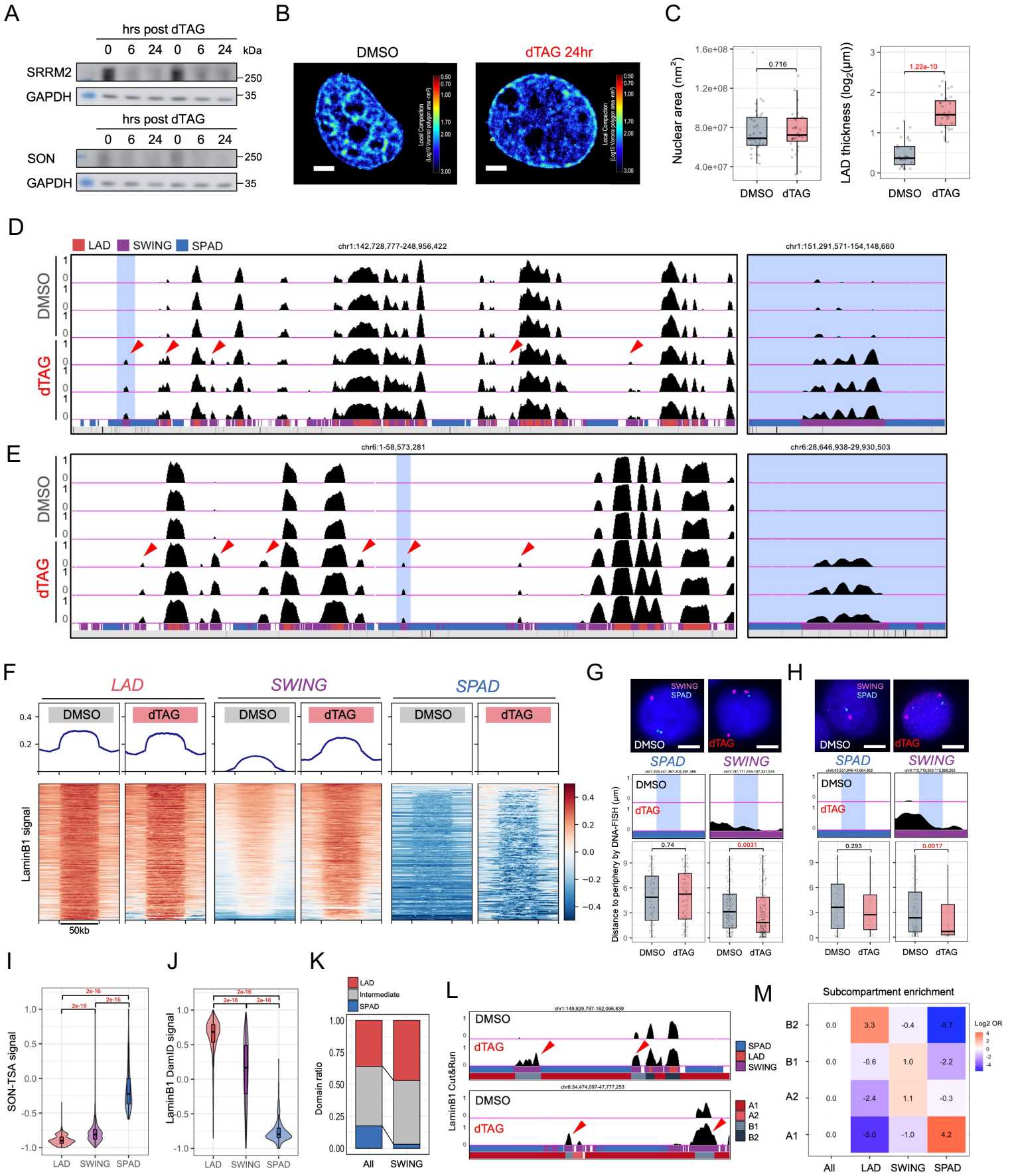
A
hrs post dTAG
0 6 24 0 6 24 kDa
SRRM2
GAPDH
250
35
hrs post dTAG
0 6 24 0 6 24
SON
GAPDH
250
35
B
DMSO
dTAG 24hr
C
Nuclear area (nm²)
0.716
DMSO dTAG
LAD thickness (log2(µm))
1.22e-10
DMSO dTAG
D
LAD SWING SPAD
chr1:142,728,777-248,956,422
chr1:151,291,571-154,148,660
DMSO
dTAG
E
chr6:1-58,573,281
chr6:28,646,938-29,930,503
DMSO
dTAG
F
LAD
SWING
SPAD
DMSO dTAG
LaminB1 signal
50kb
G
SWING SPAD
DMSO dTAG
SPAD SWING
Distance to periphery by DNA-FISH (µm)
0.74
0.0031
DMSO dTAG
H
SWING SPAD
DMSO dTAG
SPAD SWING
0.293
0.0017
DMSO dTAG
I
SON-TSA signal
2e-16
LAD SWING SPAD
J
LaminB1 DamID signal
2e-16
LAD SWING SPAD
K
LAD
Intermediate
SPAD
Domain ratio
All SWING
L
chr1:149,929,797-162,096,839
DMSO
dTAG
SPAD
LAD
SWING
chr6:34,474,097-47,777,253
A1
A2
B1
B2
LaminB1 Cut&Run
M
Subcompartment enrichment
B2 0.0 3.3 -0.4 -5.7
B1 0.0 -0.6 1.0 -2.2
A2 0.0 -2.4 1.1 -0.3
A1 0.0 -5.0 -1.0 4.2
All LAD SWING SPAD
Log2 OR

Figure1

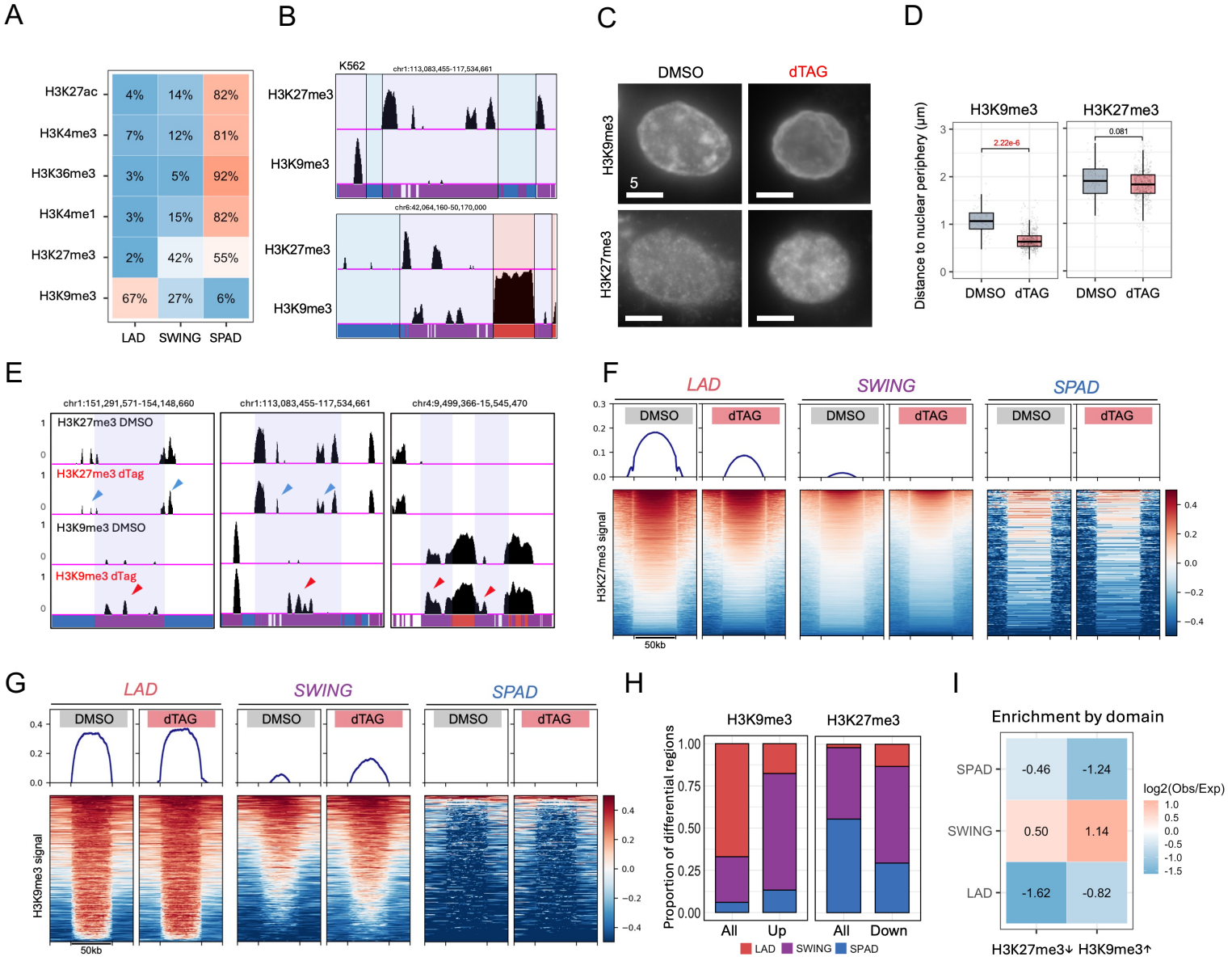
A
H3K27ac 4% 14% 82%
H3K4me3 7% 12% 81%
H3K36me3 3% 5% 92%
H3K4me1 3% 15% 82%
H3K27me3 2% 42% 55%
H3K9me3 67% 27% 6%
LAD SWING SPAD
B
K562
chr1:113,083,455-117,534,661
H3K27me3
H3K9me3
chr6:42,064,160-50,170,000
H3K27me3
H3K9me3
C
DMSO
dTAG
H3K9me3
H3K27me3
5
D
H3K9me3
H3K27me3
2.22e-6
0.081
Distance to nuclear periphery (µm)
DMSO dTAG DMSO dTAG
E
chr1:151,291,571-154,148,660
chr1:113,083,455-117,534,661
chr4:9,499,366-15,545,470
H3K27me3 DMSO
H3K27me3 dTag
H3K9me3 DMSO
H3K9me3 dTag
F
LAD
SWING
SPAD
DMSO
dTAG
H3K27me3 signal
50kb
G
LAD
SWING
SPAD
DMSO
dTAG
H3K9me3 signal
50kb
H
H3K9me3
H3K27me3
Proportion of differential regions
All Up All Down
LAD SWING SPAD
I
Enrichment by domain
SPAD -0.46 -1.24
SWING 0.50 1.14
LAD -1.62 -0.82
log2(Obs/Exp)
H3K27me3↓ H3K9me3↑

Figure2

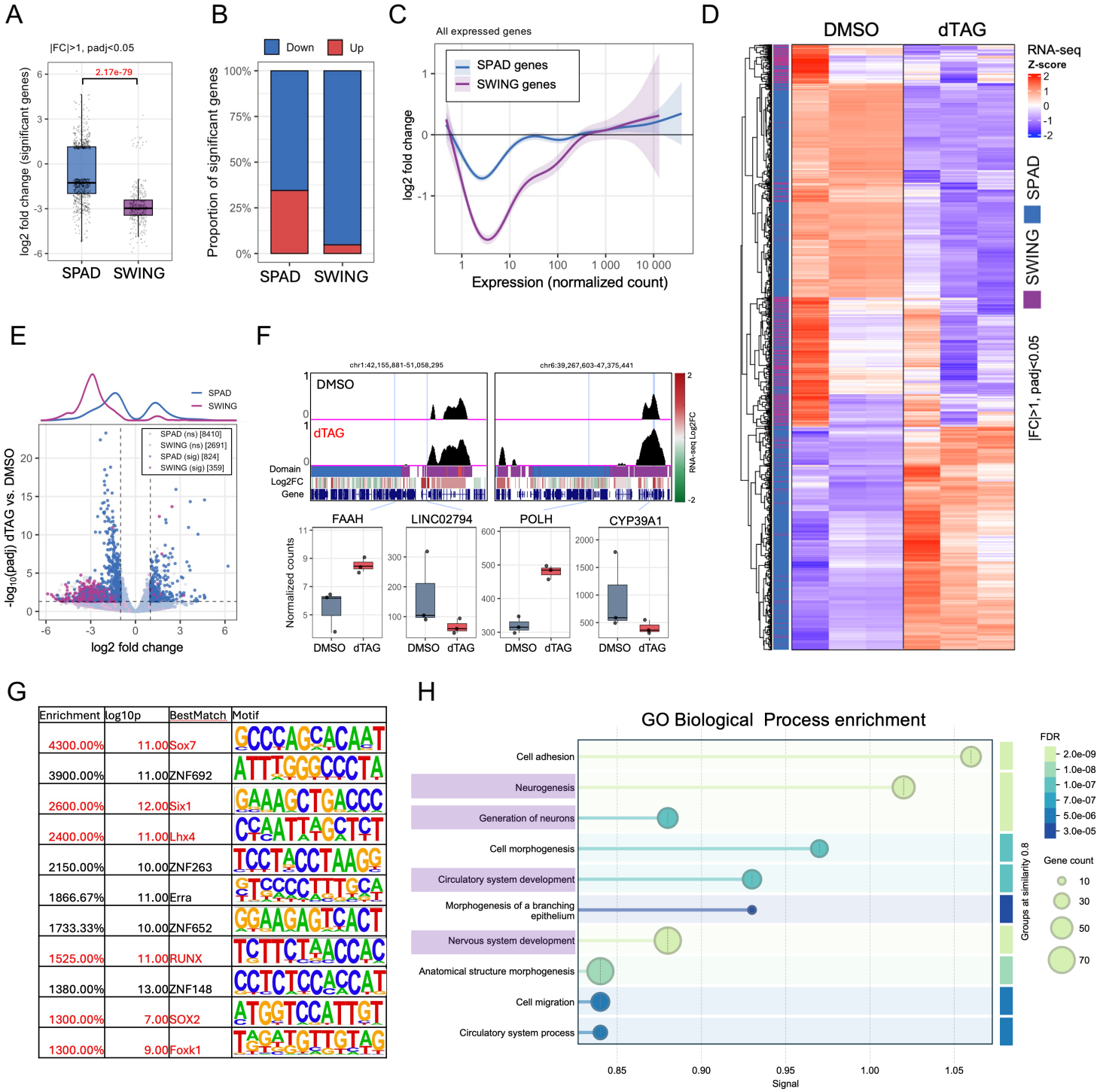

Enrichment	log10p	BestMatch	Motif
4300.00%	11.00	Sox7	
3900.00%	11.00	ZNF692	
2600.00%	12.00	Six1	
2400.00%	11.00	Lhx4	
2150.00%	10.00	ZNF263	
1866.67%	11.00	Erra	
1733.33%	10.00	ZNF652	
1525.00%	11.00	RUNX	
1380.00%	13.00	ZNF148	
1300.00%	7.00	SOX2	
1300.00%	9.00	Foxk1	

Figure3

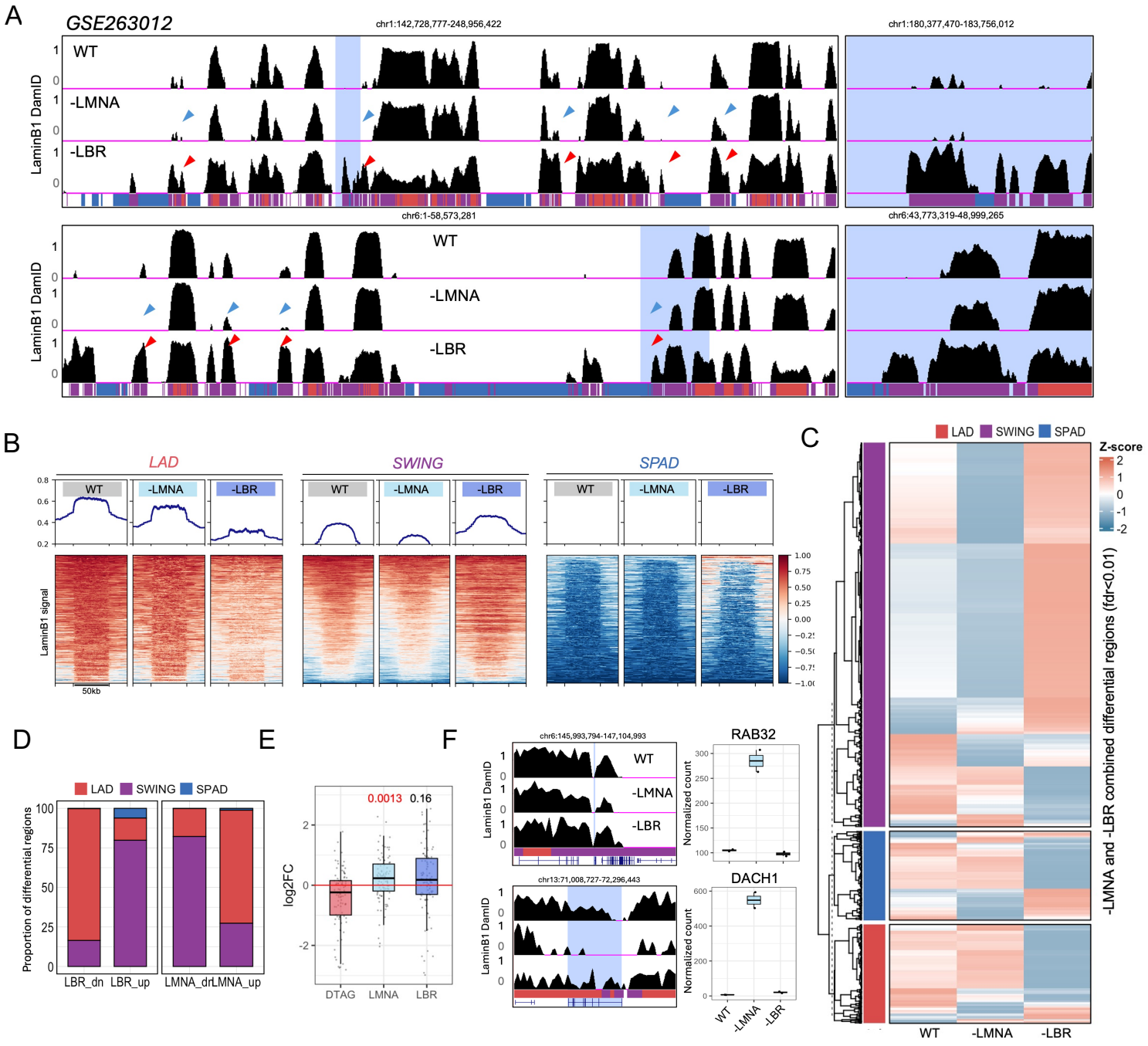
A
GSE263012
chr1:142,728,777-248,956,422
chr1:180,377,470-183,756,012
WT
-LMNA
-LBR
LaminB1 DamID
chr6:1-58,573,281
chr6:43,773,319-48,999,265
B
LAD
SWING
SPAD
LaminB1 signal
50kb
C
Z-score
-LMNA and -LBR combined differential regions (fdr<0.01)
D
Proportion of differential regions
LBR_dn
LBR_up
LMNA_dr
LMNA_up
E
0.0013
0.16
log2FC
DTAG
LMNA
LBR
F
chr6:145,993,794-147,104,993
chr13:71,008,727-72,296,443
RAB32
DACH1
Normalized count

Figure4

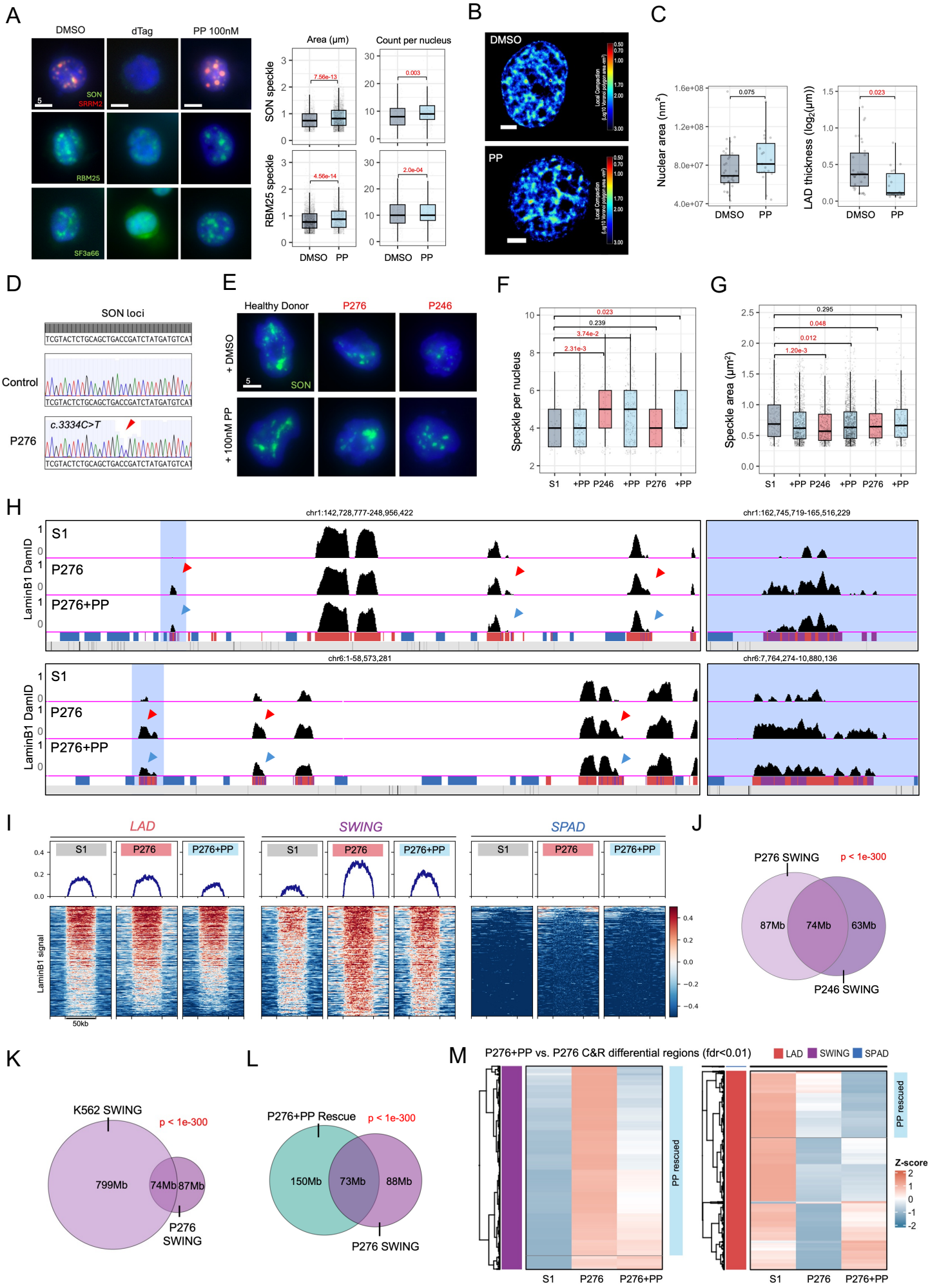
A
DMSO
dTag
PP 100nM
SON
SRRM2
RBM25
SF3a66
Area (µm)
Count per nucleus
SON speckle
RBM25 speckle
7.56e-13
0.003
4.56e-14
2.0e-04
DMSO
PP
B
DMSO
PP
C
Nuclear area (nm²)
LAD thickness (log₂(µm))
0.075
0.023
D
SON loci
Control
P276
c.3334C>T
E
Healthy Donor
P276
P246
+ DMSO
+ 100nM PP
SON
F
Speckle per nucleus
0.023
0.239
3.74e-2
2.31e-3
S1
+PP
P246
P276
G
Speckle area (µm²)
0.295
0.048
0.012
1.20e-3
H
chr1:142,728,777-248,956,422
chr1:162,745,719-165,516,229
chr6:1-58,573,281
chr6:7,764,274-10,880,136
LaminB1 DamID
S1
P276
P276+PP
I
LAD
SWING
SPAD
LaminB1 signal
50kb
J
P276 SWING
p < 1e-300
87Mb
74Mb
63Mb
P246 SWING
K
K562 SWING
p < 1e-300
799Mb
74Mb
87Mb
P276 SWING
L
P276+PP Rescue
p < 1e-300
150Mb
73Mb
88Mb
P276 SWING
M
P276+PP vs. P276 C&R differential regions (fdr<0.01)
LAD
SWING
SPAD
PP rescued
Z-score

Figure5

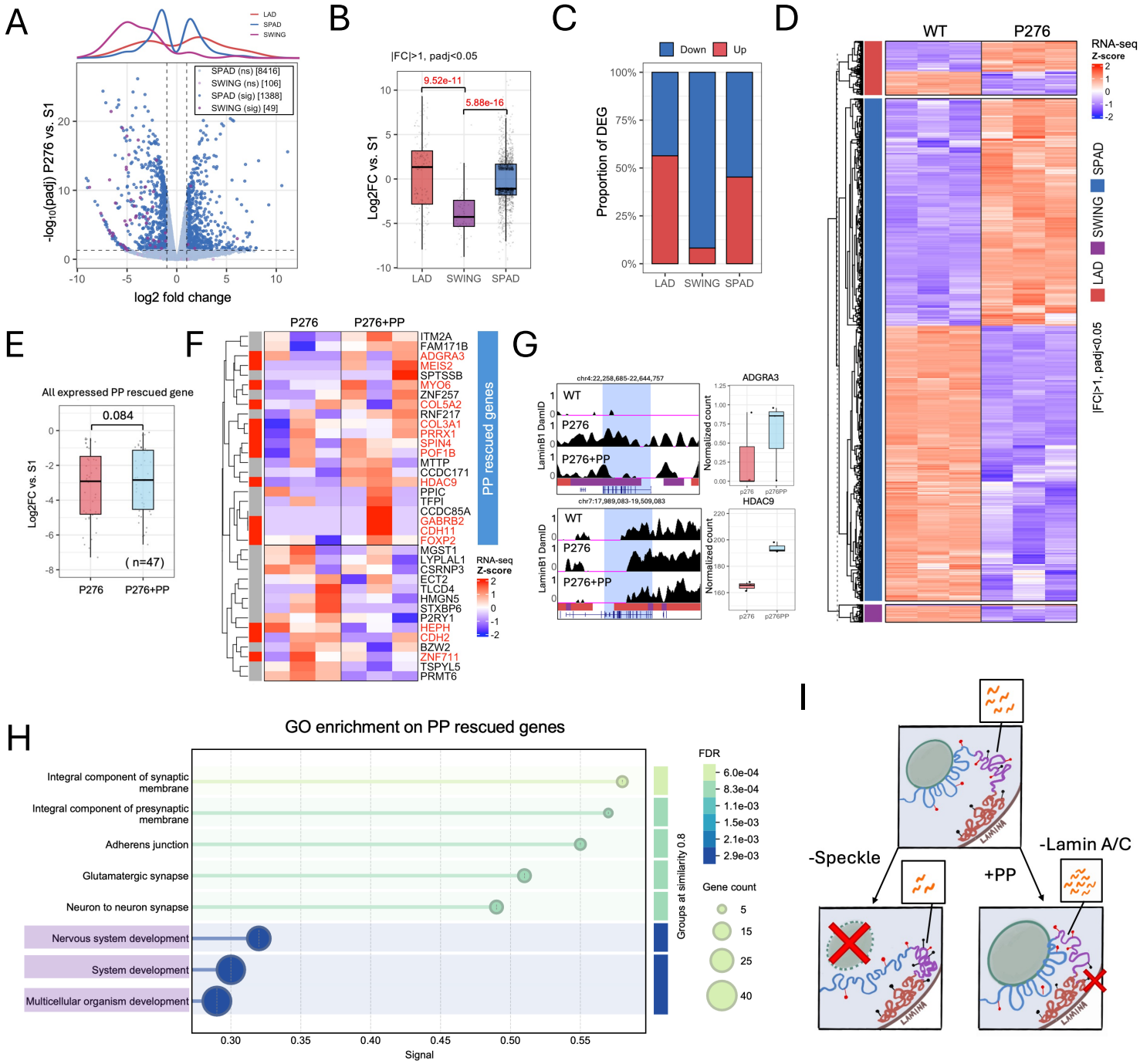
A
LAD
SPAD
SWING
SPAD (ns) [8416]
SWING (ns) [106]
SPAD (sig) [1388]
SWING (sig) [49]
-log10(padj) P276 vs. S1
log2 fold change
B
|FC|>1, padj<0.05
9.52e-11
5.88e-16
Log2FC vs. S1
LAD
SWING
SPAD
C
Down
Up
Proportion of DEG
100%
75%
50%
25%
0%
LAD
SWING
SPAD
D
WT
P276
RNA-seq
Z-score
SPAD
SWING
LAD
|FC|>1, padj<0.05
E
All expressed PP rescued gene
0.084
Log2FC vs. S1
(n=47)
P276
P276+PP
F
P276
P276+PP
ITM2A
FAM171B
ADGRA3
MEIS2
SPTSSB
MYO6
ZNF257
COL5A2
RNF217
COL3A1
PRRX1
SPIN4
POF1B
MTTP
CCDC171
HDAC9
PPIC
TFPI
CCDC85A
GABRB2
CDH11
FOXP2
MGST1
LYPLAL1
CSRNP3
ECT2
TLCD4
HMGN5
STXBP6
P2RY1
HEPH
CDH2
BZW2
ZNF711
TSPYL5
PRMT6
PP rescued genes
RNA-seq
Z-score
G
chr4:22,258,685-22,644,757
WT
P276
P276+PP
LaminB1 DamID
ADGRA3
Normalized count
p276
p276PP
chr7:17,989,083-19,509,083
HDAC9
H
GO enrichment on PP rescued genes
Integral component of synaptic membrane
Integral component of presynaptic membrane
Adherens junction
Glutamatergic synapse
Neuron to neuron synapse
Nervous system development
System development
Multicellular organism development
Groups at similarity 0.8
FDR
6.0e-04
8.3e-04
1.1e-03
1.5e-03
2.1e-03
2.9e-03
Gene count
5
15
25
40
Signal
I
-Speckle
+PP
-Lamin A/C
LAMINA

Figure6

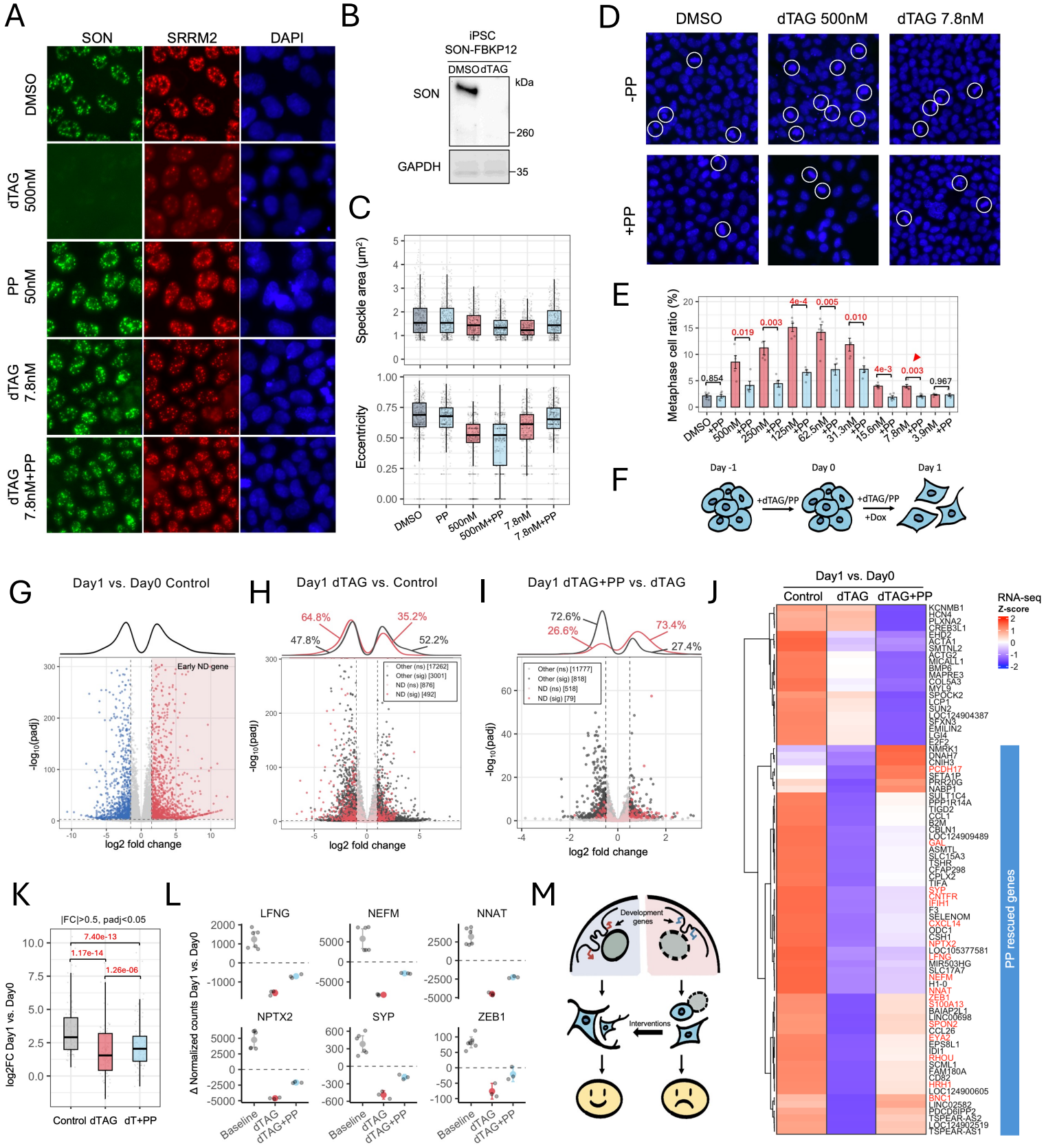
A
SON
SRRM2
DAPI
DMSO
dTAG 500nM
PP 50nM
dTAG 7.8nM
dTAG 7.8nM+PP
B
iPSC
SON-FBKP12
DMSO dTAG
SON
kDa
260
GAPDH
35
C
Speckle area (μm²)
Eccentricity
DMSO
PP
500nM
500nM+PP
7.8nM
7.8nM+PP
D
DMSO
dTAG 500nM
dTAG 7.8nM
-PP
+PP
E
Metaphase cell ratio (%)
0.854
0.019
0.003
4e-4
0.005
0.010
4e-3
0.003
0.967
DMSO
+PP
500nM
250nM
125nM
62.5nM
31.3nM
15.6nM
7.8nM
3.9nM
F
Day -1
Day 0
Day 1
+dTAG/PP
+dTAG/PP
+Dox
G
Day1 vs. Day0 Control
Early ND gene
-log10(padj)
log2 fold change
H
Day1 dTAG vs. Control
64.8%
35.2%
47.8%
52.2%
Other (ns) [17262]
Other (sig) [3001]
ND (ns) [876]
ND (sig) [492]
I
Day1 dTAG+PP vs. dTAG
72.6%
26.6%
73.4%
27.4%
Other (ns) [11777]
Other (sig) [818]
ND (ns) [518]
ND (sig) [79]
J
Day1 vs. Day0
Control
dTAG
dTAG+PP
RNA-seq
Z-score
PP rescued genes
K
|FC|>0.5, padj<0.05
7.40e-13
1.17e-14
1.26e-06
log2FC Day1 vs. Day0
Control
dTAG
dT+PP
L
LFNG
NEFM
NNAT
NPTX2
SYP
ZEB1
Δ Normalized counts Day1 vs. Day0
Baseline
dTAG
dTAG+PP
M
Development genes
Interventions

Figure7